Accepted Manuscript

The 2016 Mw 6.0 Hutubi earthquake: a blind thrust event along the northern Tian Shan front

Xiaohang Wang, Caijun Xu, Yangmao Wen, Shuai Wang, Guangyu Xu, Zhuohui Xiao, Lihua Fang

PII: S1367-9120(19)30015-X
DOI: https://doi.org/10.1016/j.jseaes.2019.01.011
Reference: JAES 3747

To appear in: *Journal of Asian Earth Sciences*

Received Date: 24 July 2018
Revised Date: 20 December 2018
Accepted Date: 6 January 2019

Please cite this article as: Wang, X., Xu, C., Wen, Y., Wang, S., Xu, G., Xiao, Z., Fang, L., The 2016 Mw 6.0 Hutubi earthquake: a blind thrust event along the northern Tian Shan front, *Journal of Asian Earth Sciences* (2019), doi: https://doi.org/10.1016/j.jseaes.2019.01.011

The 2016 Mw 6.0 Hutubi earthquake: a blind thrust event along the northern Tian Shan front

Xiaohang Wang[a], Caijun Xu[a,b,c,*], Yangmao Wen[a,b,c], Shuai Wang[a], Guangyu Xu[a], Zhuohui Xiao[a] and Lihua Fang[d]

a School of Geodesy and Geomatics, Wuhan University, Wuhan, China

b Key Laboratory of Geospace Environment and Geodesy, Ministry of Education, Wuhan University, Wuhan, China

c Collaborative Innovation Center of Geospatial Technology, Wuhan University, Wuhan, China

d Institute of Geophysics, China Earthquake Administration, Beijing, China

* Correspondence: cjxu@sgg.whu.edu.cn; Tel.: +86-27-6877-8805

Abstract

The Tian Shan Range, which trends E-W along the southern margin of the Junggar Basin, is one of the longest and most active intracontinental orogenic belts in central Asia. On 8 December 2016 (05:15:04 UTC), a Mw 6.0 earthquake ruptured the northern Tian Shan front. Here, we use Sentinel-1 radar imagery to investigate the deformation and source parameters related to this event. The co-seismic surface deformation was predominated by uplift without surface rupture. Ascending and descending interferograms indicate that the event triggered small co-seismic deformations with maximum line-of-sight displacements of 22 mm and 24 mm, respectively. Although the north-dipping and south-dipping plane solutions can both fit the observations well, the north-dipping solution with a dip of 58° is preferred in consideration of the relocated aftershocks and regional geological structure. Significant slip is located between depths of 12 km and 17 km, suggesting that the event was caused by a completely blind thrust fault. This blind rupture is characterized largely by a compact thrusting patch with a peak slip of 56 cm at a depth of 13 km. The source model generates a geodetic moment of 6.678×10^{17} Nm corresponding to a Mw 5.85 event. Both the interferometric synthetic aperture radar modeling and the aftershock locations indicate that the rupture plane is linked to the Huoerguosi-Manas-Tugulu fault at a depth of ~16 km, a typical locking depth in the Tian Shan. We suggest that the 2016 Hutubi earthquake more likely occurred on a back-thrust of the Huoerguosi-Manas-Tugulu fault, and the back-thrust is interpreted to represent a preexisting normal fault beneath the Qigu anticline belt that was tectonically inverted during the Cenozoic.

Keywords: radar interferometry; Tian Shan; Hutubi earthquake; rupture model; thrust faulting; seismic hazard

1. Introduction

On 8 December 2016 (05:15:04 UTC), a moderate earthquake with a magnitude of Mw 6.0 (U.S. Geological Survey [USGS], 2016; see Data and Resources) occurred in the Hutubi area of the Xinjiang Uyghur Autonomous Region of China. This event did not lead to the loss of life, but it caused hundreds of buildings to collapse and generated vast economic losses. No surface rupture was found near the epicenter according to a field investigation conducted shortly thereafter (Lu et al., 2017). The focal mechanism solution from the USGS indicates that this event was purely composed of thrust faulting. Two nodal plane solutions were provided by USGS with a strike, dip and rake of 269°/71°/93° and

80°/19°/81°. In addition, the epicenter (43.83° N and 86.35° E) was located ~100 km west of the city of Urumqi at a depth of 17.6 km. A total of 1431 shocks in the wake of this event were recorded by local seismic networks as of December 13 (China Earthquake Networks Center, 2016; see Data and Resources), and the maximum moment magnitude of the aftershocks was Mw 4.0.

The harsh natural conditions of the region led to many difficulties during geological surveys and geophysical data acquisition in the field. The closest continuously monitoring GPS site to the epicenter is located 40 km away; consequently, the co-seismic deformation of the event was obviously not observed (GNSS Data Products of the China Earthquake Administration, 2016; see Data and Resources). Fortunately, with the development of the interferometric synthetic aperture radar (InSAR) technique, we are able to acquire high-accuracy and high-resolution near-field deformation measurements without any ground control points, and thus, this approach provides an effective way to obtain surface deformation of the 2016 Hutubi earthquake (Wen et al., 2016; Xu et al., 2016; Wang et al., 2017; Xu et al., 2018).

In this study, ascending and descending Sentinel-1 radar images were used to measure the near-field co-seismic deformation related to the 2016 Hutubi earthquake. Then, the nonlinear multipeak particle swarm optimization (MPSO) algorithm and linear least-square method were used to calculate the fault geometry parameters and slip distribution (Feng et al., 2010). Furthermore, we discussed the possible rupture plane of this event on the basis of relocated aftershocks and the local geological structure. Finally, the static Coulomb failure stress (CFS) triggered by this event was evaluated to investigate the stress state in the surrounding area.

2. Geological background

The Tian Shan Range (Figure 1), one of the most active mountain building belts in central Asia, borders the Tarim Basin to the south and the Junggar Basin to the north (Gong et al., 2016). This mountain range extends east-west over more than 2500 km from the Xinjiang Uygur Autonomous Region of China in the east to Kazakhstan in the west with a north-south width of 250 - 350 km (Deng et al., 2000). Quaternary studies have constrained the long-term amount and rate of shortening of this region to 13.5 - 14.6 km and 4.62 - 5.0 mm/yr, respectively, since 2.92 Ma (Yang et al., 1997; Burchfiel et al., 1999; Deng et al., 2000; Fu et al., 2003). The present-day slip rate derived from GPS is 4 - 6 mm/yr, which is consistent with geological results (Yang et al., 2008; Wang et al., 2011).

The northern Tian Shan constitutes the northern foreland fold-thrust belt of the actively uplifting Tian Shan Range, which represents a northern extension of the active Himalayan orogeny (Tapponnier et al.,

1979) and may be potentially associated with Arabian convergent tectonics (Yin, 2010). Orogenic processes are always accompanied by crustal shortening, and the strata in this region are intensively deformed by Cenozoic folding and faulting (Tapponnier et al., 1979). Most historical earthquakes in the northern Tian Shan were dominated by earthquakes generated along blind thrust faults (Deng et al., 1994) characterized by a rapid decay of the rupture displacement with a deep hypocenter and the lack of obvious surface deformation.

The 2016 Hutubi earthquake occurred in the Urumqi piedmont depression, a Mesozoic-Cenozoic foreland basin in the northern Tian Shan. Three approximately east-west striking sub-parallel anticline belts known as the Qigu, Huoerguosi-Manas-Tugulu (HMT) and Dushanzi-Anjihai (DSZ-AJH) anticline belts from south to north were formed during the Late Cenozoic in the northern Tian Shan piedmont (Deng et al., 1996; Burchfiel et al., 1999; Fu et al., 2003). The locking depth in the Urumqi piedmont depression is 16 ± 3 km (Liu et al., 2016), which is consistent with the focal depth of the 2016 Hutubi earthquake according to the USGS. An analysis of industrial seismic reflection data and field observations indicates that these structures exhibit complex internal geometries characterized by coeval fore-thrusts and back-thrusts forming imbricated structural wedges (Avouac et al., 1993). The northern Tian Shan is an earthquake-prone area, both the 2016 Mw 6.0 Hutubi earthquake and the 1906 M 7.7 Manas earthquake occurred in the fold-thrust belt of the northern Tian Shan (Figure 1). The epicenter of the M 7.7 Manas earthquake was adjacent to the Junggar southern margin fault (JSF); however, co-seismic rupture and uplift were found along the active HMT anticline belt. The HMT fault dips to the south at ~45° from the surface and then levels out as a flat detachment fault within the Eocene and Cretaceous strata. Then, the HMT fault dips to the south at ~22° and intersects Jurassic and pre-Jurassic strata (Lu et al., 2017). The geometry of HMT fault is a typical example of fault-bend folding with a ramp-flat-ramp structure (Suppe, 1983). Moreover, it has been proposed that the HMT fault was the source of the Manas earthquake (Avouac et al., 1993; Zhang et al., 1994; Yang et al., 1997).

3. InSAR observations

3.1. SAR data processing and method

During the Hutubi earthquake, several SAR images were collected by satellites from space. C-band (5.6 cm) Sentinel-1 data (Table 1) in terrain observation with progressive scans (TOPS) mode were used to investigate the co-seismic surface deformation of the Hutubi event in this paper.

The line-of-sight (LOS) surface displacements were obtained by the two-pass differential InSAR (DInSAR) method using the Switzerland GAMMA software (Werner et al., 2001). All interferograms were generated from single look complex (SLC) products. The multi-look number in the range and azimuth were set to 10:2 to suppress noise. To avoid phase jumps between subsequent bursts, a co-registration accuracy of at least 0.001 pixels was required to eliminate the influence of along-track Doppler centroid variation in TOPS mode (Zan et al., 2006). In this paper, two methods were used to obtain high-quality co-registration images: a method considering the scene topography effects and a spectral diversity method (Scheiber and Moreira, 2000) considering the interferometric phase of the burst overlap region. Once a high-quality co-registration result between the TOPS SLC data was achieved, the topographic phase was removed using a Shuttle Radar Topography Mission (SRTM) three arc-second (90 m) digital elevation model (DEM). Then, a power spectrum filter (Goldstein and Werner, 1998) was used for the interferograms to reduce phase noise, and both interferograms were unwrapped using the branch-cut method (Goldstein et al., 2016). In addition, because of the small surface deformation associated with the Hutubi earthquake, an empirical approach involving the estimation of the best linear fit of the topography-correlated atmospheric delays attributable to the atmospheric phase screen (APS) (Bekaert et al., 2015) was used to weaken atmospheric contributions.

Finally, the interferograms were geocoded into WGS84 geographic coordinates with a resolution of 90 m.

3.2. Co-seismic deformation

Co-seismic deformation fields from ascending and descending tracks of Sentinel-1 images are shown in Figure 2. The entire deformation field caused by the Hutubi earthquake is encompassed within the SAR images. The surface deformation can be clearly observed on the interferograms due to the dry desert conditions with little vegetation in the northern Tian Shan. The deformation pattern exhibits an elliptical shape with non-detectable surface rupture, suggesting a thrust-dominated event. The ascending and descending interferograms both indicate a small amount of deformation caused by this event with maximum LOS displacements of 22 mm and 24 mm, respectively. As shown in Figures 2 (c) and (d), main coseismic deformation is concentrated in the area with large topographic relief. We believe that the coseismic deformation of the 2016 Hutubi earthquake is consistent with the orogenic mechanism of the region. Moreover, there are no sharp offsets in in the LOS profiles, which suggest a typical blind fault folding event (Stein and King, 1984).

The main errors, such as the orbital errors and topography-correlated atmospheric delays, were removed. However, some un-modeled errors remained within the interferograms. Hence, we used a 1D covariance function (Hanssen, 2001) in the non-deforming areas to describe the uncertainty. The standard deviations were 2.7 mm and 3.3 mm (Table 1) for the T014A and T094D interferograms, respectively; consequently, we can presume that the deformation field mainly contained co-seismic deformation caused by the Hutubi earthquake.

It is worth noting that there is a significant sinking signal on the north side of the HMT fault (Region X in Figure S1(a)). We found out that there is a chemical plant in this area through Google Maps. Therefore, we believe that the signal is caused by the factory production activities. In order to confirm our speculation, we processed the InSAR data from January 2016 to June 2017 in this region. As shown in Figures S1(b) and (c), surface subsidence also occurred in this area form January 12 to February 5 and from December 13, 2016 to January 6, 2017. So we believe that the deformation is not related to the 2016 Hutubi earthquake.

4. InSAR modeling

To improve the inversion efficiency, we used a resolution-based quadtree method (Lohman and Simons, 2005) to downsample the original interferograms, resulting in 294 and 375 data points for the ascending and descending pairs, respectively (Figure S2). The relative weight ratio of the ascending and descending datasets were both set to 1:0.86 based on the empirical errors derived from the 1D covariance function (Hanssen, 2001).

4.1. Fault geometry

In this study, we determined the source parameters using the analytical solutions of a rectangular dislocation in a homogeneous, elastic half-space (Okada, 1992) while assuming a Poisson ratio of 0.25. During the modeling, a nonlinear inversion scheme was adopted to determine the fault geometry parameters, and a linear inversion was performed to estimate the slip distribution along the modeled fault plane (Li et al., 2013). Here, both a north-dipping fault model and a south-dipping fault model were established due to the possibility of backthrusting. The MPSO algorithm (Feng et al., 2013) was used to invert the fault geometry parameters, including the strike, dip, slip, length, width and depth, by minimizing the misfits between the observations and the model predictions. A Monte Carlo bootstrap simulation technique (Wright et al., 1999) was employed to estimate the uncertainties and the trade-offs of the model parameters (Figures S3 and S4). Model solutions from 100 simulations perturbed with noise from the statistical properties based on previous 1-D covariance functions were used to estimate the standard deviation from their distributions. The source parameters and their 1-sigma errors are listed in Table 2. In general, the errors are relatively small. Regardless of which nodal plane is the primary fault plane, our estimates of the strike, dip and rake from the north-dipping model agree better with the determinations of other organizations than those from the south-dipping model.

4.2. Distributed slip inversion

To obtain a more physically reasonable solution, a linear inversion scheme was adopted to obtain the slip distribution along the fault plane. However, previous studies (Burgmann, 2002; Fukahata and Wright, 2008) suggested that the fault geometry parameters (especially the dip angle) obtained from a uniform slip model are not optimal for a distributed slip model. In this study, the grid search method proposed by Feng et al. (2013) was used to determine the optimal dip angle and smoothing factor simultaneously. In this method, a log function $f(\delta,\kappa^2)=\log(\psi+\xi)$ was used, where δ is the dip angle, ψ is the model roughness and ξ is the residual. Figures S5(a) and S6(a) show the changing trends of the model roughness and residual with variations in the smoothing weight for the north-dipping model and the south-dipping model, respectively. Figure S5(b) shows that the optimal dip angle and smoothing factor for the north-dipping model are 58° and 1, respectively, while those for the south-dipping model are 31° and 1 (Figure S6(b)).

Once the optimal fault geometry and smoothing factor were determined, we inverted the slip distributions for both nodal planes based on the classic linear-elastic dislocation theory. In this study, we extended the fault length and width in the north-dipping model to 20 km along the strike and 25 km along the down-dip direction, respectively, and the same dimensions in the south-dipping model were extended to 30 km and 40 km. As shown in Figures 3 and S7, the slip distributions of the north-dipping and south-dipping models both indicate a thrust-dominated event, and the ruptures did not reach the ground surface. The predominant slip occurred along the fault at depths of 12 - 17 km with a peak magnitude of 56 cm for the north-dipping model and at depths of 13 - 16 km with a peak magnitude of 47 cm for the south-dipping model. The total released geodetic moments were 6.678×10^{17} Nm (Mw 5.84) and 6.902×10^{17} Nm (Mw 5.85) for the north-dipping and south-dipping models, respectively, which are consistent with the solutions provided by the IGCEA.

The slip patches are very deep (12 - 17 km deep for the north-dipping model and 13-16km deep for the south-dipping model). So we performed a checkerboard test that retains model parameterization same as for the above inversion but different slip patterns. The checkerboard method is widely used to evaluate the resolution of slip model (Fielding et al., 2013). We synthesized displacements for InSAR samples based on a hypothesized event with a uniform slip of 0.5 m located on a 7×9 km^2 subfault patch for north-dipping model with a total of geodetic moment of 3.77×10^{18} Nm (~Mw 6.3) (Figure S8(a)). And 0.4 m located on the 8×10 km^2 subfault patch for south-dipping model with a total of geodetic moment of 1.92×10^{18} Nm (~Mw 6.2) (Figure S8(c)).

Then we inverted slip models (Figures S8(b) and (d)) for the synthetic event for a comparison. The differences between the input and output slip models indicate that our InSAR data have the capability to retrieve the movement at such depth.

4.3. Inversion results

Figures 4 and S9 show the simulated deformations and residuals for the north-dipping and south-dipping slip models. It is clear that the co-seismic deformation for both ascending and descending pairs can be sufficiently explained by the distributed slip model. The north-dipping model exhibits root-mean-square errors (RMSEs) of approximately 2.8 mm and 3.1 mm for the ascending and descending data, respectively, and the south-dipping model exhibits corresponding RMSEs of 2.9 mm and 3.4 mm, which are comparable to the noise levels of InSAR observations. Therefore, it is difficult to determine the primary nodal plane according to similarities between RMSEs.

Hence, the use of only InSAR observations cannot distinguish the primary nodal plane in this study. As a result, a blind thrust event is suggested, and our InSAR modeling provides two nodal plane solutions with a strike, dip and rake of 270°/58°/93° for the north-dipping fault model and 87°/31°/85° for the south-dipping fault model. The optimal nodal plane is further constrained in the next section.

5. Discussion

5.1. Dip orientation

It is always challenging from geodetic data to determine dip orientation for a buried reverse earthquake at small or moderate size (Lohman et al., 2002; Lohman and Barnhart, 2010). Consequently, other evidence is required, such as relocated aftershocks and synthetic seismological data. After the Hutubi earthquake, the Xinjiang Earthquake Administration set up two temporary stations near the epicenter (~10 km). The temporary stations effectively improved the azimuthal coverage of stations and the accuracy of earthquake location. In this study, the phase data recorded by the Xinjiang Seismic Network and temporary stations deployed around the Hutubi earthquake source region were integrated to relocate the aftershock sequence of this event. By 23:59 PM on January 31, a total of 2316 aftershocks were recorded. In order to get reliable relocation results, we mainly used the phase data within 400 km of the epicentral distance. The locations of 622 aftershocks were determined using a double-difference location algorithm (Waldhauser and Ellsworth, 2000; Fang et al., 2015). As shown in Figure 5(a), the aftershock sequence attenuates rapidly, indicating a typical major aftershock event. The aftershocks (Figure 5(d)) outline a north-dipping profile with a dip angle of ∼58°, which is the best-fitting dip angle for the north-dipping model.

To further distinguish the primary nodal plane, synthetic seismological data were employed to determine the dip orientation. Figure 6 shows the geological interpretation of seismic profile A-A' (Figure 1) (Lu et al., 2017) and provides detailed information on the geological and structural framework of the northern Tian Shan front. We found that the hypocenter of the Hutubi earthquake was located near the HMT fault at a depth of 16 km. The geometry of the HMT fault, which corresponds to a ramp-flat-ramp structure, dips toward the south with the unusually low dip of 22°. Compared with the south-dipping model established by our InSAR observations, it is possible that the seismogenic fault of the Hutubi earthquake was the HMT fault. However, few aftershocks were distributed along the HMT fault (Figure 6), suggesting that the Hutubi earthquake likely did not occur along the main fault of the HMT anticline belt.

Based on seismic reflection surveys, Guan et al. (2016) found that several active thrust sheets with steep dips (45°-55°) are distributed throughout the Tian Shan. An example is the north-dipping fault A in Figure 6, above which the Qigu anticline is developed. This phenomenon, which constitutes a common structural style throughout the Tian Shan region, was interpreted to represent preexisting normal faults that have been inverted to accommodate regional tectonic shortening during the

Cenozoic (Sibson and Xie, 1998; Guan et al., 2016). Based on the mechanism and location of the Hutubi event, we infer that an inverted normal fault is connected to the HMT fault at depth under the Qigu anticline belt, and this fault (back-thrust) may represent the seismogenic fault of the 2016 Hutubi earthquake. In conclusion, we prefer the north-dipping model because it is consistent with the relocated aftershocks and the tectonic context.

Similar to the Hutubi event, the 2015 Mw 6.4 Pishan (China) earthquake, occurred in the foreland fold-and-thrust belt in the western Kunlun Shan, is a blind, reverse-faulting event (He et al., 2016). The geological structures in these two regions are very similar, with thrust faults and a low dip fault plane. The Pishan event occurred on the low dip fault plane (21°) which is very similar to the HMT fault (22°) and rheology contrast across the northern boundary of the Tibetan Plateau is likely to be responsible for the low dip angle of the Pishan fault plane (Ainscoe et al., 2017). However, the Hutubi earthquake more likely occurred on the back-thrust of the low dip HMT fault. Both of these thrust events may have a great relationship with the collision between the Indian and Eurasian plates. But there may be some differences due to the geometric complexity.

5.2. Static Coulomb stress changes

Many research investigations have revealed that the static Coulomb stress change caused by a main shock can trigger subsequent rupture events (Toda et al., 1998; Parsons et al., 1999; Xa, 2004). After the 2016 Hutubi earthquake, part of the accumulated stress was released due to the rupture of the seismogenic fault, and the remainder of the stress was transmitted throughout the surrounding areas, resulting in an aggregation of stress in the study region (King et al., 1994). Increasing the Coulomb stress may promote fault rupture activity, while a decrease in the Coulomb stress, representing stress release, inhibits rupture (Harris and Simpson, 1998). Although the Coulomb stress following an event is relatively smaller than the tectonic stress required for an earthquake, events can be sufficiently triggered by a low Coulomb stress of 0.01Mpa (King et al., 1994; Ziv and Rubin, 2000).

To understand the stress transfer from deep to shallow depths during the earthquake, we adopted the static Coulomb failure stress change (ΔCFS) (King et al., 1994) to estimate the state of stress around the seismogenic zone. The Matlab-based software Coulomb v3.3 (Toda and Stein, 2005) was employed to calculate the co-seismic static Coulomb stress change triggered by the Hutubi earthquake. The effective coefficient of friction and the shear modulus were set to 0.4 and

3.32×10^{10} N/m^2 (Steck and Phillips, 2009), respectively. Figure 7(a) shows the △CFS based on the north-dipping model at a depth of 11 km (the top boundary of the main slip asperity) for a receiver fault with a strike of 270°, a dip of 58° and a rake of 93°. In addition, we also show another two profiles at different depth in Figure S10 The results reveal that the stresses decreased in the main rupture area and increased in the southern region of the main rupture. The aftershocks were concentrated in the regions of an increased Coulomb stress change (Figure 7), providing additional evidence that the seismogenic fault slopes toward the north.

We also constructed a cross-section perpendicular to the north-dipping rupture fault of the Hutubi earthquake. The results indicate that this event exhibited an increased static Coulomb stress loading on the shallower section (S1) (Figure 7(b)), which may have brought it closer to future failure. Considering the seismogenic tectonic conditions, Yang et al. (1998) suggested that it is difficult to generate Mw ≥ 6 earthquakes in the shallow parts of the northern Tian Shan front. Therefore, the earthquake-prone shallower section (S1) might experience several earthquakes in the future, but it will not likely generate strong earthquakes. This conclusion is based on the back-thrusting branch extends to the shallower segment. If it is just a new short branch of HMT and the branch did not extend to the shallow segment of S1. More detailed information is required to analyze the seismic hazard. However, the active HMT fault is capable of producing much larger earthquakes (e.g., the 1906 M 7.7 Manas earthquake) (Lu et al., 2017). Therefore, considering the possible impact of the Hutubi event on it, the HMT fault is worthy of particular attention.

6. Conclusions

The surface deformation caused by the Hutubi earthquake and mapped using Sentinel-1 data reveals that the maximum displacements were 22 mm and 24 mm along the lines of sight of the ascending and descending tracks, respectively. Inversion results show that the slip distributions of this earthquake are dominated by a pure thrust fault. The north-dipping solution is preferred considering relocated aftershocks and the local geological structure. Our results demonstrate that the peak co-seismic slip (56 cm) occurred at a depth of 13 km on a north-dipping fault with a dip of 58°. The total released moment was 6.678×10^{17} Nm, which is equivalent to a Mw 5.85 earthquake. Both the InSAR modeling and the aftershock locations indicate that the rupture plane was linked to the HMT fault at a depth of ~16 km. We suggest that the 2016 Hutubi earthquake more likely occurred on a back-thrust of the HMT fault, and the back-thrust is interpreted to represent a preexisting normal fault beneath the Qigu anticline belt that was tectonically inverted during the Cenozoic.

Data and resources

The U.S. Geological Survey (USGS) National Earthquake Information Center (NEIC) moment tensors were obtained from https:// earthquake.usgs.gov/earthquakes/eventpage/us 20007 z2r#executive (last accessed December 2016).

The Global Navigation Satellite System (GNSS) data products from the China Earthquake Administration for the 2016 Hutubi Earthquake were found at http://www.cgps.ac.cn/cgs/viewArticleNormal.action?id=323 (last accessed December 2016).

The information for the 2016 Hutubi earthquake from the China Earthquake Networks Center (CENC) was downloaded from http://www.csi.ac.cn/manage/eqDown/05 LargeEQ/201612 081315 M6.2/ zonghe.html (last accessed December 2016).

The research data and models in this paper are shared here https://data.mendeley.com/submissions/ees/edit/mt2h969xwy?submission_id=JAES_94192&token=232fe725-78c9-455d-8365-3bb412d057dd.

Acknowledgments

This work is supported by the National Natural Science Foundation of China (key program) under Grants No.41431069, the National Natural Science Foundation of China under Grants No. 41574002, No. 41721003 and No. 41774011, the DAAD Thematic Network Project under Grant No. 57173947. The Sentinel-1 SAR data were provided by the European Space Agency (ESA) through the Sentinels Scientific Data Hub. We thank Renqi Lu from the Institute of Geology, China Earthquake Administration for his helpful discussion and for providing the seismic reflection profile. Some figures in this paper were prepared using Generic Mapping Tools (Wessel and Smith, 1998; Wessel et al., 2013).

References

Ainscoe, E. A., Elliott, J. R., Copley, A., Craig, T. J., Li, T., Parsons, B. E., &Walker, R. T. (2017). Blind thrusting, surface folding, and the development of geological structure in the Mw 6.3 2015 Pishan (China) earthquake. Journal of Geophysical Research: Solid Earth, 122, 9359-9382. https://doi.org/10.1002/2017JB014268

Avouac J P, Tapponnier P, Bai M, et al (1993), Active thrusting and folding along the northern Tian Shan and Late Cenozoic rotation of the Tarim relative to Dzungaria and Kazakhstan, Journal of Geophysical Research Solid Earth, 98(B4), 6755-6804.

Bekaert D P S, Walters R J, Wright T J, et al (2015), Statistical comparison of InSAR tropospheric correction techniques, Remote Sensing of Environment, 170, 40-47.

Burchfiel B C, Brown E T, Deng Q D, et al (1999), Crustal Shortening on the Margins of the Tian Shan, Xinjiang, China, International Geology Review, 41(8), 665-700.

Burchfiel, B. C., E. T. Brown, Q. Deng, X. Feng, J. Li, P. Molnar, J. Shi, Z. Wu, and H. You (1999), Crustal shortening on the margins of the Tian Shan, Xinjiang, China, International Geology Review, v. 41, p. 665–700.

Burgmann R (2002), Deformation during the 12 November 1999 Duzce, Turkey, Earthquake, from GPS and InSAR Data, Bulletin of the Seismological Society of America, 92(1), 161-171.

Deng Q, Fang X, Zhang P, et al (2000), Active Tectonic of Tian Shan, Seismological Press, Beijing.

Deng Q, Zhang P, Xu X, et al (1996), Paleoseismology of the northern piedmont of Tian Shan Mountains, northwestern China, Journal of Geophysical Research Solid Earth, 101(B3), 5895-5920.

Deng, Q. D., X. Y. Feng, X. P. Yang (1994), Study on Holocene paleoearthquake by large trench in the Manas-Tugulu reverse faultand-fold zone along Northern margin of the Tian Shan mountain in Xinjiang[A] in Research on Active Faults, Institute of Geology, SSB (Editor), Vol. 3, Seismological Press, Beijing, China (in Chinese).

England, P., & Molnar, P. (2005). Late Quaternary to decadal velocity fields in Asia. Journal of Geophysical Research, 110, B12401. https://doi.org/10.1029/2004JB003541

Fang L H, Jian-Ping W U, Wang W L et al (2015), Relocation of the 2014 Ms 7.3 earthquake sequence in Yutian, Xinjiang, Chinese Journal of Geophysics, 58(3), 802-808.

Feng W, Li Z, Elliott J R, et al (2013), The 2011 MW 6.8 Burma earthquake: fault constraints provided by multiple SAR techniques, Geophysical Journal International, 195(1), 650-660.

Feng W, Li Z (2010), A novel hybrid PSO/simplex algorithm for determining earthquake source parameters using InSAR observations, Progress in Geophysics, 25(4), 1189-1196.

Fielding, E. J., A. Sladen, Z. Li, J. P. Avouac, R. Bürgmann, I. Ryder (2013), Kinematic fault slip evolution source models of the 2008 M7. 9 Wenchuan earthquake in China from SAR interferometry, GPS and teleseismic analysis and implications for Longmen Shan tectonics, Geophys. J. Int., 194, 1138-1166.

Fu B, Lin A, Kano K I, et al (2003), Quaternary folding of the eastern Tian Shan, northwest China, Tectonophysics, 369(1), 79-101.

Fukahata Y, Wright T J (2008), A non-linear geodetic data inversion using ABIC for slip distribution on a fault with an unknown dip angle, Geophysical Journal of the Royal Astronomical Society, 173(2), 353-364.

Goldstein R M, Werner C L (1998), Radar interferogram filtering for geophysical applications, Geophysical Research Letters, 25(21), 4035-4038.

Goldstein R M, Zebker H A, Werner C L (2016), Satellite radar interferometry: Two-dimensional phase unwrapping, Radio Science, 2016, 23(4), 713-720.

Gong Z, Li S H, Li B (2016), Late Quaternary faulting on the Manas and Hutubi reverse faults in the northern foreland basin of Tian Shan, China, 2016, 212-225.

Guan, S. W., J. M. Stockmeyer, J. H. Shaw, A. Plesch, and J. Zhang (2016), Structural inversion, imbricate wedging, and out-of-sequence thrusting in the southern Junggar fold-and-thrust belt, northern Tian Shan, China, AAPG Bulletin 100, no. 9, 1443–1468.

Hanssen, R.F (2001), Radar Interferometry: Data Interpretation and Error Analysis; Kluwer Academic Publishers: Dordrecht, The Netherlands.

Harris R A, Simpson R W (1998), Suppression of large earthquakes by stress shadows: A comparison of Coulomb and rate ‐ and ‐ state failure, Journal of Geophysical Research Solid Earth, 103(B10), 24439-24451.

He P, Wang Q, Ding K, et al (2016), Source model of the 2015 Mw 6.4 Pishan earthquake constrained by interferometric synthetic aperture radar and GPS: Insight into blind rupture in the western Kunlun Shan, Geophysical Research Letters, 43(4), 1511-1519.

King G C P, Stein R S, Lin J (1994), Static stress changes and the triggering of earthquakes, Bull.seism.soc.am, 78(3), 935-953.

Li Z, Feng W, Xu X, et al (2013), The 1998 Mw 5.7 Zhangbei-Shangyi earthquake revisited: a buried thrust fault revealed with interferometric synthetic aperture radar, Geochemistry, Geophysics, Geosystems, 9(4), 532-553.

Liu D Q, Liu M, Wang H T, et al (2016), Slip rates and seismic moment deficits on major faults in the Tian Shan region, Chinese Journal of Geophysics.

Lohman R B, Barnhart W D (2010), Evaluation of earthquake triggering during the 2005–2008 earthquake sequence on Qeshm Island, Iran, Journal of Geophysical Research Solid Earth, 115(B12), 956-988.

Lohman R B, Simons M, Savage B (2002), Location and mechanism of the Little Skull Mountain earthquake as constrained by satellite radar interferometry and seismic waveform modeling, Journal of Geophysical Research Solid Earth, 107(B6), ETG-1-ETG 7-10.

Lohman, R.B., Simons, M (2005), Some thoughts on the use of InSAR data to constrain models of surface deformation: Noise structure and data downsampling. Geochem. Geophys. Geosyst, 6, 359-361.

Lu R, He D, Xu X, et al (2017), Seismotectonics of the 2016 Hutubi M 6.2 earthquake: Implications for the 1906 Manas M 7.7 earthquake in the northern Tian Shan mountain belt, China, Seismological Research Letters.

Okada, Y (1992), Internal deformation due to shear and tensile faults in a half-space. Bull. Seismol. Soc. Am, 82, 1018-1040.

Parsons T, Stein R S, Simpson R W, et al (1999), Stress sensitivity of fault seismicity: A comparison between limited‐offset oblique and major strike‐slip faults, Journal of Geophysical Research Solid

Earth, 104(B9), 20183-20202.

Scheiber R, Moreira A (2000), Coregistration of interferometric SAR images using spectral diversity, IEEE Transactions on Geoscience & Remote Sensing, 38(5), 2179-2191.

Sibson R H, Xie G (1998), Dip range for intracontinental reverse fault ruptures: Truth not stranger than friction, Bulletin of the Seismological Society of America, 88(4), 1192-1198.

Steck L K, Phillips W S, Mackey K, et al (2009), Seismic tomography of crustal P and S across Eurasia, Geophysical Journal of the Royal Astronomical Society, 177(1), 81-92.

Stein R S, King G C (1984), Seismic potential revealed by surface folding: 1983 coalinga, california, earthquake, Science, 224(4651), 869-872.

Stein R S, Yeats R S (1989), Hidden Earthquakes, Scientific American, 260(6), 48-57.

Suppe J (1983). Geometry and kinematics of fault-bend folding, Am. J. Sci. 283, 684-721.

Tapponnier, P., and P. Molnar (1979), Active faulting and Cenozoic tectonics of the Tian Shan, Mongolia, and Baykal regions: Journal of Geophysical Research, v. 84, no. B7, p. 3425-3459

Toda S, Stein R S, Reasenberg P A, et al (1998), Stress transferred by the 1995 Mw 6.9 Kobe, Japan, shock: Effect on aftershocks and future earthquake probabilities, Journal of Geophysical Research Solid

Earth, 103(B10), 24543-24565.

Toda S, Stein R S, Richards−Dinger K, et al (2005), Forecasting the evolution of seismicity in southern California: Animations built on earthquake stress transfer, Journal of Geophysical Research Solid Earth, 110(B5), 26521-26542.

Waldhauser F, Ellsworth W L (2000), A Double-Difference Earthquake Location Algorithm: Method and Application to the Northern Hayward Fault, California, Bulletin of the Seismological Society of America, 90(90), 1353-1368.

Wang H, Liu M, Gao J, Shen X, Zhang G (2011), Slip rates and seismic moment deficits on major active faults in mainland China, J. Geophys. Res, 116, B02405, http://dx.doi.org/10.1029/2010JB007821.

Wang H, Liuzeng J, Ng A H M, et al (2017), Sentinel-1 observations of the 2016 Menyuan earthquake: A buried reverse event linked to the left-lateral Haiyuan fault, International Journal of Applied Earth Observation & Geoinformation, 61, 14-21.

Wang S, Xu C, Wen Y, et al (2017), Slip Model for the 25 November 2016 Mw 6.6 Aketao Earthquake, Western China, Revealed by Sentinel-1 and ALOS-2 Observations, Remote Sensing, 9(9).

Wen Y, Xu C, Liu Y, et al (2016), Deformation and Source Parameters of the 2015 Mw 6.5 Earthquake in Pishan, Western China, from

Sentinel-1A and ALOS-2 Data, Remote Sensing, 8(2), 134.

Werner C, Wegmller U, Strozzi T et al (2001), GAMMA SAR and interferometric processing software, Proc. ERS-Envisat Symposium, Gothenburg, 2001.

Wessel, P., Smith, W.H.F., (1998), New, improved version of generic mapping tools released. Eos. Trans. AGU 79, 579.

Wessel, P., Smith, W.H.F., Scharroeo, R., Luis, J., Wobbe, F., (2013), Generic mapping tools: improved version released. Eos Trans. AGU 94, 409-410.

Wright T J, Parsons B E, Jackson J A, et al (1999), Source parameters of the 1 October 1995 Dinar (Turkey) earthquake from SAR interferometry and seismic bodywave modelling, Earth & Planetary Science Letters, 172(1-2), 23-37.

Xa A M, Freed (2004), EARTHQUAKE TRIGGERING BY STATIC, DYNAMIC, AND POSTSEISMIC STRESS TRANSFER, Annual Review of Earth & Planetary Sciences, 33(33), 335-367.

Xu, C., Gong, Z., Niu, J., (2016), Recent developments in seismological geodesy. Geod. Geodyn, (7), 157-164.

Xu G, Xu C, Wen Y (2018), Sentinel-1 observation of the 2017 Sangsefid earthquake, northeastern Iran: Rupture of a blind reserve-slip fault near the Eastern Kopeh Dagh, Tectonophysics.

Yang S, Li J, Wang Q (2008), Study on Tian Shan recent deformation and faulting by GPS, Sci. China 38 (7), 872-880.

Yang X P, Deng Q D, Zhang P Z, et al (1998), Estimation of structure and potential source area of active fault-fold belt in the northern Tian Shan area, Seismology and Geology, 20 (3), 193-200 (in Chinese).

Yang, X., Deng, Q., Feng, X., Zhang, P., Xu, X., & Li, J. (1997), Active reverse fault- fold zones and the site prediction of large earthquakes along northern Tian Shan, Xinjiang, China. Inland Earthquake.

Yin, A., (2010), Cenozoic tectonic evolution of Asia: A preliminary synthesis: Tectonophysics, v. 488, p. 293-325, doi: 10.1016/j.tecto.2009.06.002.

Yuhu M, Liu W, Wang P, et al (2012), Characteristics and anomaly of earthquake sequence activity of Da Qaidam M_S6.3 and M_S6.4 in 2008 and 2009[J]. Earthquake Research in China, 28(2), 188-199.

Zan F D, Guarnieri A M M (2006), TOPSAR: Terrain Observation by Progressive Scans, IEEE Transactions on Geoscience & Remote Sensing, 44(9), 2352-2360.

Zhang, P. Z., Q. D. Deng, X. W. Xu, S. Z. Peng, X. Y. Feng, X. P. Yang, R. B. Zhao, and J. Li (1994), Blind thrust, folding earthquake, and the 1906 Manas earthquake, Xinjiang, Seismol. Geol, 16, 193-203(in Chinese).

Zhi min L I, Hong wei T U, Tian Q J, et al (2010), The 2008 Ms 6.3 earthquake in the Dacaidan region, Qinghai province and its seismotectonic setting, Progress in Geophysics, 25(3), 768-774.

Ziv, A.; Rubin, A.M. (2000), Static stress transfer and earthquake triggering: No lower threshold in sight? J. Geophys. Res., 105, 13631-13642.

Table 1. Details of Sentinel-1 images used in this study

Satellite	Track	Master	Slave	Perp. B	Inc.	Azi.	σ[†]	α[‡]
		YYYYMMDD	YYYYMMDD	m	°	°	mm	km
Sentinel-1A	T014A	20161119	20161213	-59	33.8	-10.7	2.7	11.3
Sentinel-1B	T094D	20161124	20161218	38	33.8	-169.3	3.3	6.1

† Standard deviation calculated with all points in the non-deforming area.

‡ E-folding correlation length scale of the 1D covariance function.

Table 2. Source parameters of the 2016 Hutubi earthquake.

Model*	North-dipping			South-dipping			Depth† (km)	Mw‡
	Strike (°)	Dip (°)	Rake (°)	Strike (°)	Dip (°)	Rake (°)		
USGS	269	71	93	80	19	81	17.6	6.0
IGCEA	273	70	108	49	27	50	18	5.85
CENC	277	69	88	103	21	96	19	6.0
This study	268 ±1.12	57 ±0.49	93 ±1.09	87 ±3.07	29 ±0.96	85 ±2.34	15.8/15.2 ±0.34/±0.25	5.84/5.85

* Institute of Geophysics, China Earthquake Administration (IGCEA); China Earthquake Networks Center (CENC).

† The depth of our models represents the center of the fault plane; 15.8 is for the north-dipping model; 15.2 is for the south-dipping model.

‡ 5.84 is for the north-dipping model; 5.85 is for the south-dipping model.

Highlights:

(1) Small amplitude deformation due to a range front earthquake is detected from the SAR data.

(2) Source parameters inversion shows that this earthquake is a blind thrust event.

(3) Multiple-source data lead support that this earthquake occurred on a back-thrust of the HMT fault.

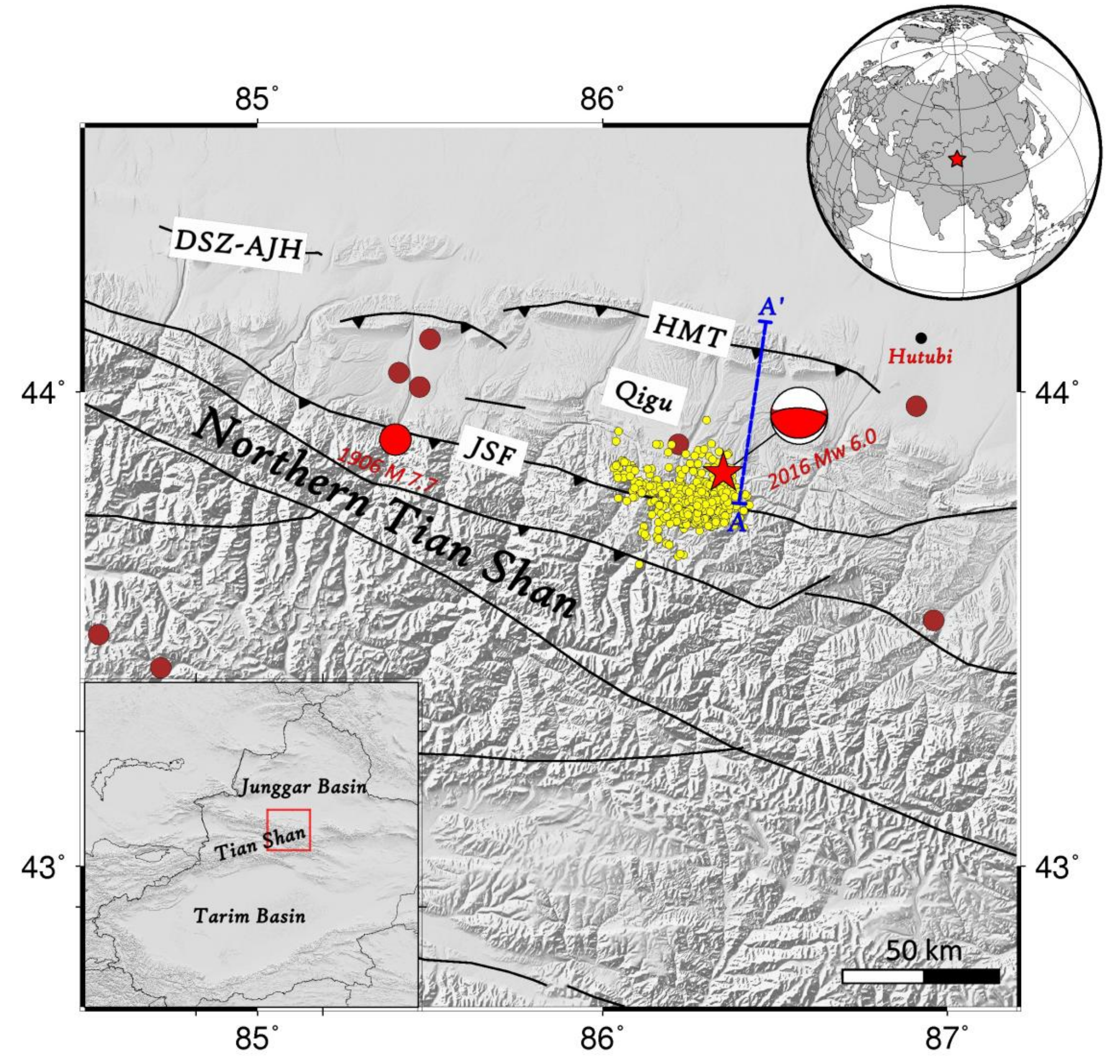

85°
86°
87°
44°
43°
DSZ-AJH
HMT
A'
A
Hutubi
Qigu
JSF
Northern Tian Shan
1906 M 7.7
2016 Mw 6.0
Junggar Basin
Tian Shan
Tarim Basin
50 km

Figure Captions

Figure 1. Tectonic setting of the northern Tian Shan, northwestern China. The focal mechanism of the 2016 Hutubi earthquake is from the USGS. Yellow circles are the aftershocks from the Xinjiang Seismic Network between 8 December 2016 and 20 December 2016. The red star is the epicenter of the 2016 Hutubi earthquake. The red circle is the epicenter of the 1906 Manas earthquake. Brown circles are historic earthquakes (magnitude ≥ 5.0) in this area. The blue line A-A’ corresponds to a combined industrial seismic reflection profile. Black lines represent major faults in the northern Tian Shan. JSF: Junggar southern margin fault; Qigu: Qigu anticline belt; HMT: Huoerguosi-Manas-Tugulu fault; DSZ-AJH: Dushanzi-Anjihai anticline belt.

Figure 2. Co-seismic LOS deformation obtained from InSAR data. (a) Co-seismic deformation from Sentinel-1A ascending track T014A. (b) Co-seismic deformation from Sentinel-1B descending track T094D. Red star indicates the epicenter of the 2016 Hutubi earthquake from the USGS. (c) and (d) LOS displacements (red dashed line), simulated displacements by north-dipping uniform slip model (sky-blue dashed line) and topography (black line) along profiles A-B and C-D, respectively.

Figure 3. Slip distribution of the north-dipping model. Red dots indicate aftershocks. Red star indicates the hypocenter of the Hutubi earthquake from the USGS.

Figure 4. (a-b) Modeled co-seismic deformations and (c-d) residuals from the north-dipping distributed slip model on ascending track 014 (a and c) and descending track (b and d). The short and long arrows indicate the radar looking and flight directions, respectively.

Figure 5. Co-seismic deformation map of the epicenter area with aftershocks. (a) Magnitude-time graph of the Hutubi earthquake. (b) Main shock of the 2016 Hutubi earthquake and the aftershocks recorded from 8 to 20 December 2016. (c) Aftershocks along cross-section A-B. (d) Aftershocks along cross-section C-D. The yellow line represents the nodal plane for the north-dipping model.

Figure 6. Seismic interpretation of section A-A’ (Lu et al., 2017) in Figure 1. Fault A is regarded

as a normal fault that was tectonically inverted during the Cenozoic (Guan et al., 2016). Colored circles indicate aftershocks. HMT: Huoerguosi-Manas-Tugulu fault.

Figure 7. Calculated static Coulomb failure stress changes caused by the 2016 Hutubi earthquake with the optimal InSAR north-dipping distributed slip model. (a) The distribution of the Coulomb stress change at a depth of 11 km. Black circles indicate aftershocks at a depth of 9-13 km. (b) Cross-section of Coulomb stress change through profile A-B. Black circles indicate all aftershocks. Red star indicates the epicenter of the Hutubi earthquake from the USGS.

Figure S1. Interferograms at different time periods. (a) Interferogram 20161119-20161213, red star represents the epicenter. (b) Interferogram 20160112-20160205. (c) Interferogram 20161213-20170106. X is the sinking region. Y is another sinking region far away from the HMT fault.

Figure S2. Sampling data derived from resolution-based quadtree method. (a) Sampling data from Sentinel-1A ascending track T014A. (b) Sampling data from Sentinel-1B descending track T094D.

Figure S3. Model parameters for a north-dipping fault plane solution from the Monte-Carlo analysis. Histograms show distribution in individual model parameters.

Figure S4. Model parameters for a south-dipping fault plane solution from the Monte-Carlo analysis. Histograms show distribution in individual model parameters.

Figure S5. (a) A trade-off curve associated with the north-dipping model with a dip angle of 58°. The blue and purple lines show the trends of the model roughness and the residuals of the modeled simulations after normalizing ([ξ, ψ]), respectively, while the red line represents log ($\xi + \psi$). (b) Contour map of log ($\xi + \psi$) with variations in the dip and hyperparameter α^2. White star indicates the global minimum.

Figure S6. (a) A trade-off curve associated with the south-dipping model with a dip angle of 31°.

The blue and purple lines show the trends of the model roughness and the residuals of modeled simulations after normalizing ([ξ, ψ]), respectively, while the red line represents log ($\xi + \psi$). (b) Contour map of log ($\xi + \psi$) with variations in the dip and hyperparameter α^2. White star indicates the global minimum.

Figure S7. Slip distribution of south-dipping model; Red dots indicate aftershocks. Red star indicates the hypocenter of Hutubi earthquake from the USGS.

Figure S8. Checkerboard test. (a) Synthetic event with a uniform slip of 0.5 m located on a 7×9 km^2 subfault patch for north-dipping model. (b) Inverted slip model form (a). (c) Synthetic event with a uniform slip of 0.4 m located on a 8×10 km^2 subfault patch for south-dipping model. (d) Inverted slip model form (c).

Figure S9. (a-b) Modeled co-seismic deformations and (c-d) residuals from the south-dipping distributed slip model on ascending track 014 (a and c) and descending track 094 (b and d). The short and long arrows indicate the radar looking and flight directions, respectively.

Figure S10. Calculated static Coulomb failure stress changes caused by the 2016 Hutubi earthquake with the optimal InSAR north-dipping distributed slip model. (a) The distribution of the Coulomb stress change at a depth of 6 km. Black circles indicate aftershocks at a depth of 4-8 km. (b) The distribution of the Coulomb stress change at a depth of 16 km. Black circles indicate aftershocks at a depth of 13-17 km. Red star indicates the epicenter of the Hutubi earthquake from the USGS.

Table Captions

Table 1. Details of Sentinel-1 images used in this study

Table 2. Source parameters of the 2016 Hutubi earthquake.

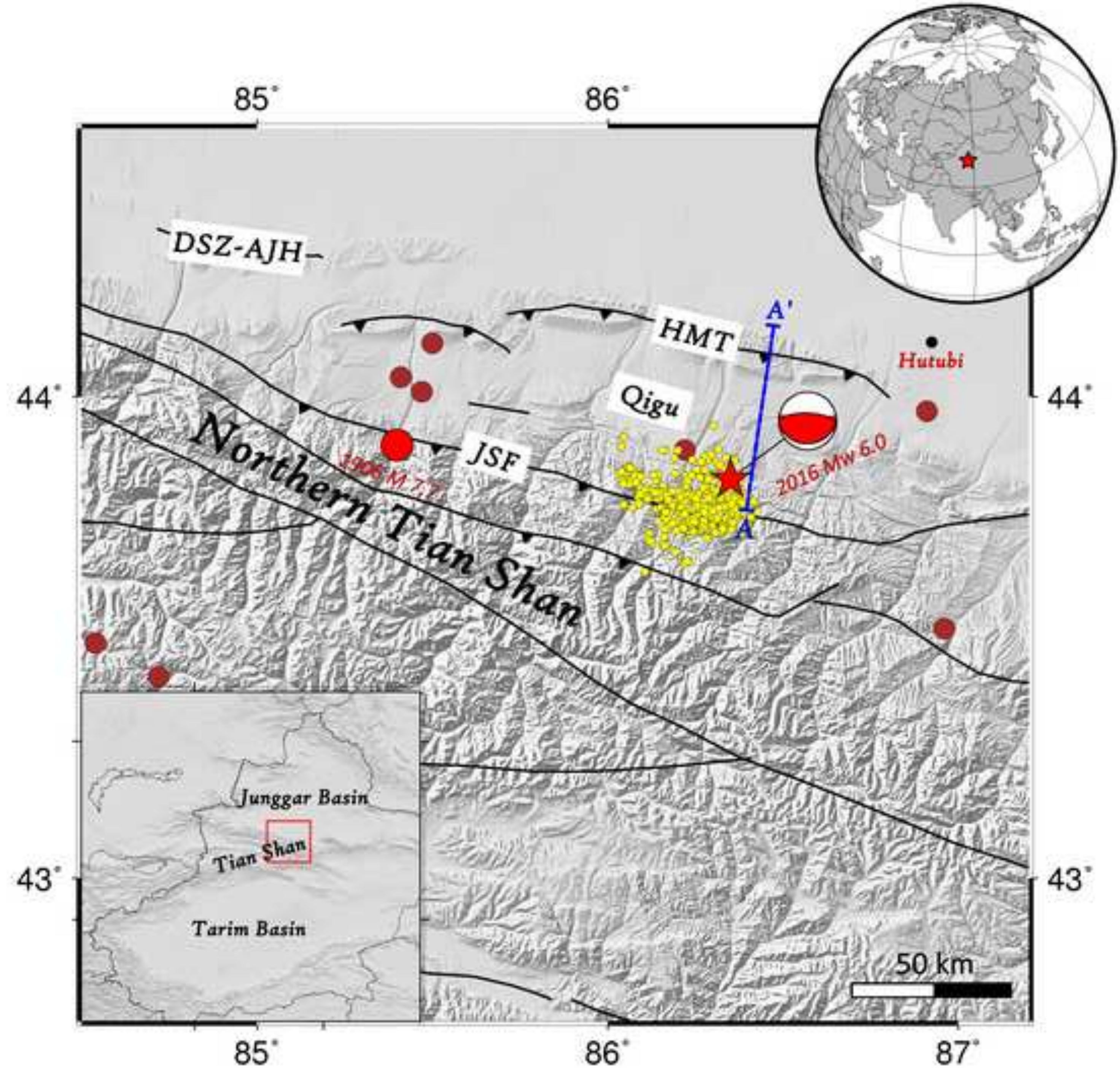
85°
86°
87°
44°
43°
DSZ-AJH
HMT
Qigu
JSF
Hutubi
A'
A
Northern Tian Shan
2016 Mw 6.0
Junggar Basin
Tian Shan
Tarim Basin
50 km

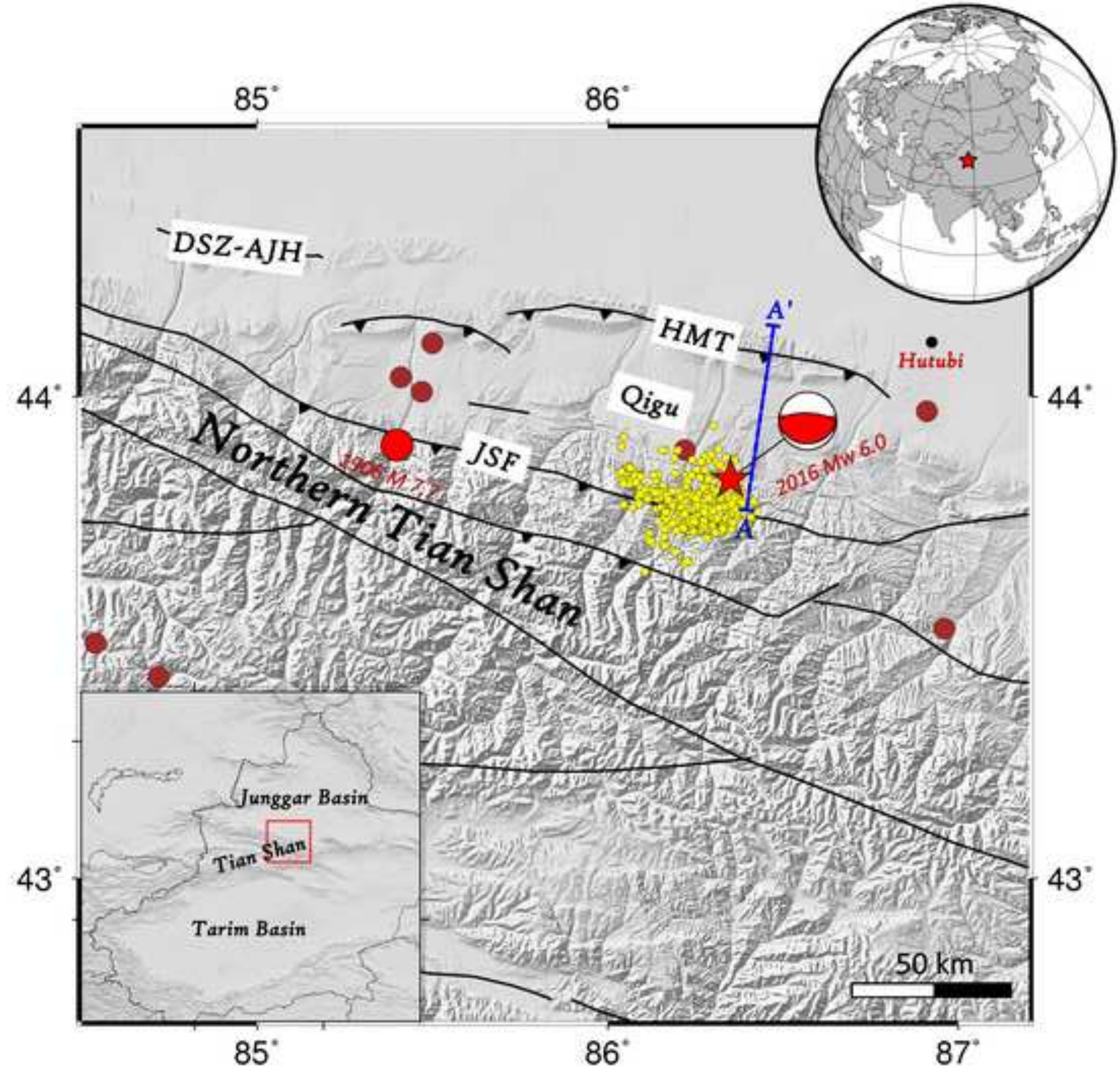
85°
86°
87°
44°
43°
DSZ-AJH
HMT
Qigu
Hutubi
JSF
Northern Tian Shan
1906 M 7.7
2016 Mw 6.0
A'
A
Junggar Basin
Tian Shan
Tarim Basin
50 km

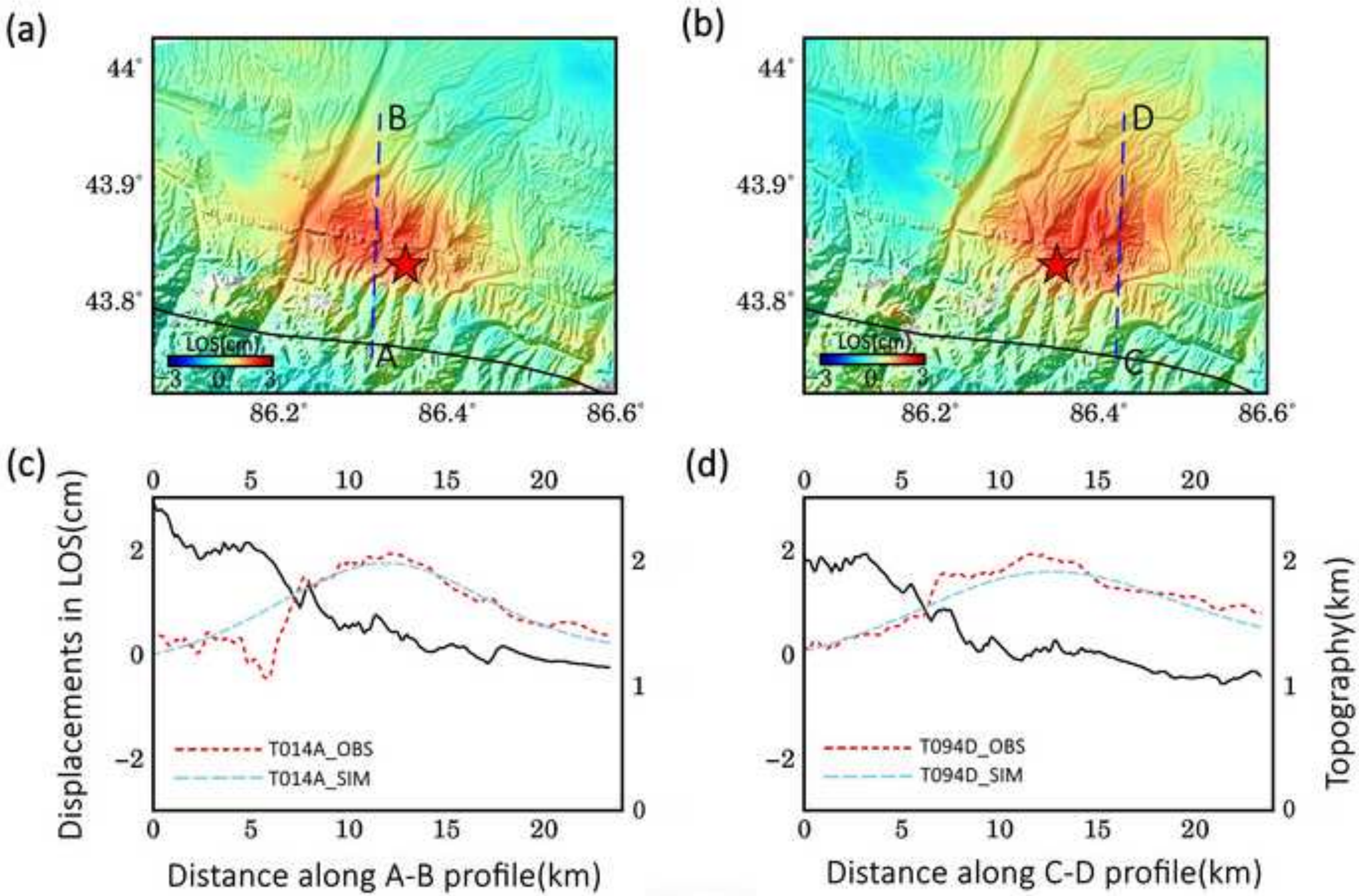
(a)
(b)
44°
43.9°
43.8°
86.2°
86.4°
86.6°
A
B
C
D
LOS(cm)
-3 0 3
(c)
(d)
Displacements in LOS(cm)
Topography(km)
T014A_OBS
T014A_SIM
T094D_OBS
T094D_SIM
Distance along A-B profile(km)
Distance along C-D profile(km)

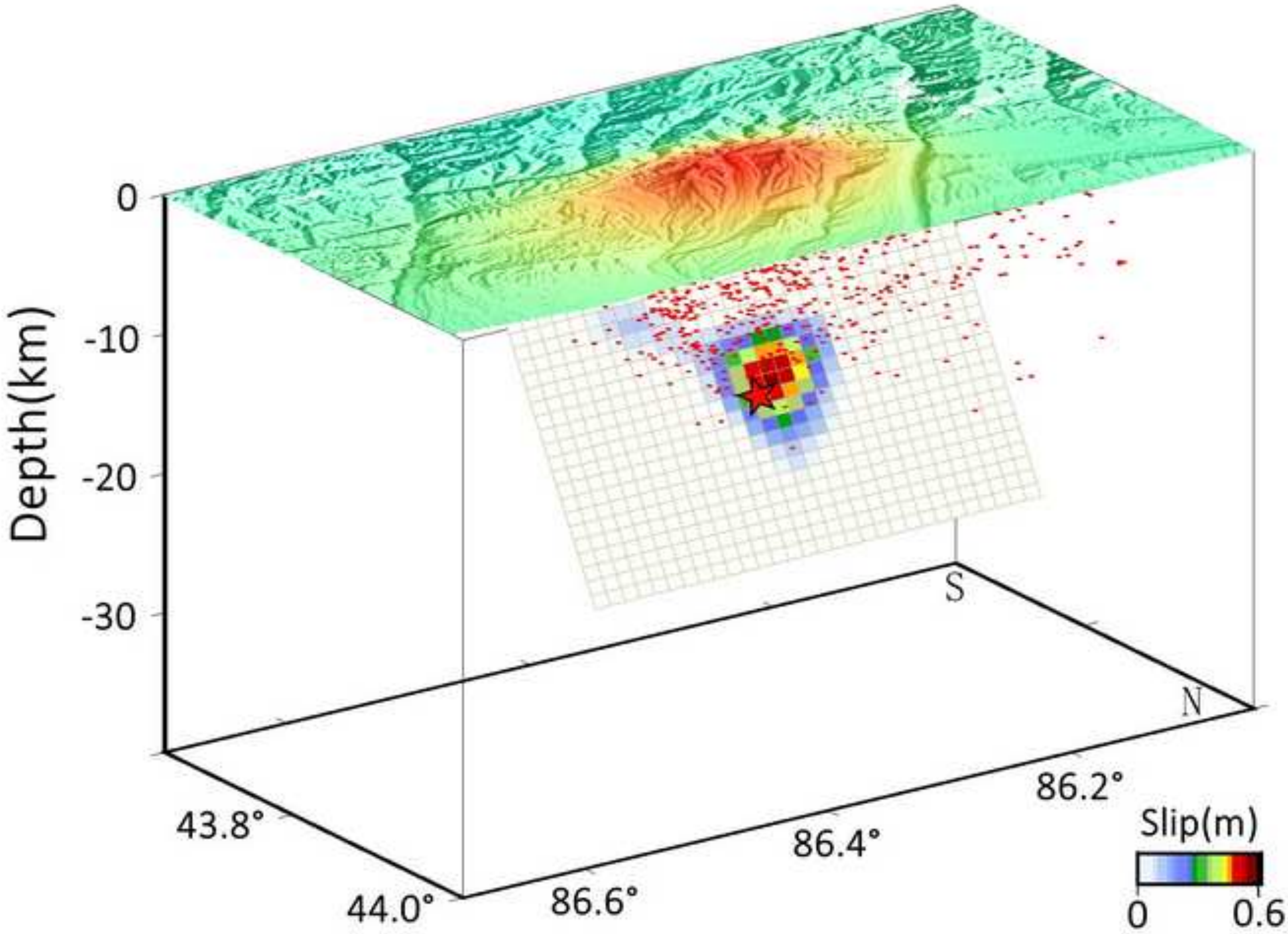

Depth(km)
0
-10
-20
-30
S
N
43.8°
44.0°
86.6°
86.4°
86.2°
Slip(m)
0
0.6

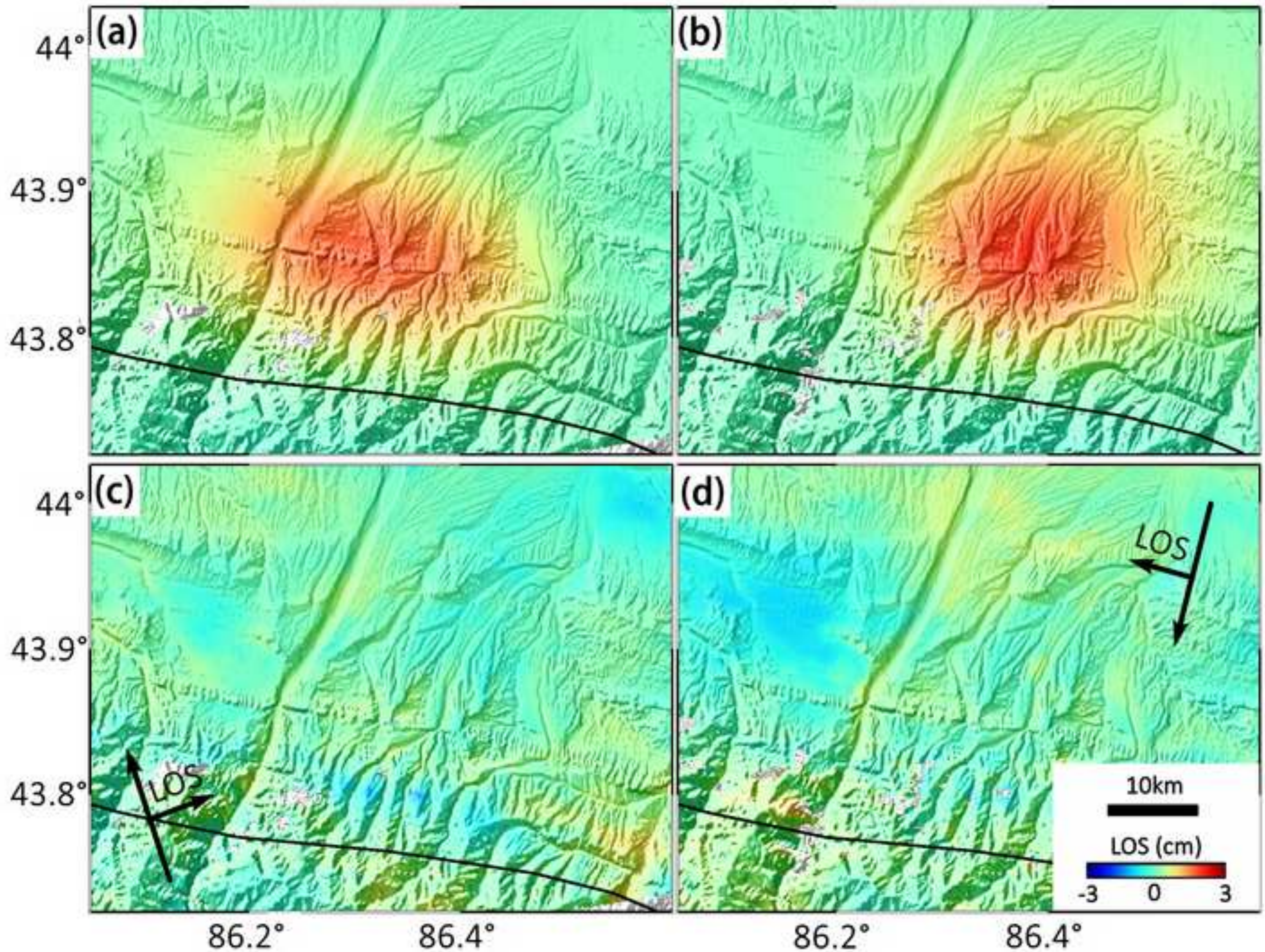

(a)
(b)
(c)
(d)
44°
43.9°
43.8°
44°
43.9°
43.8°
86.2°
86.4°
86.2°
86.4°
LOS
LOS
10km
LOS (cm)
-3
0
3

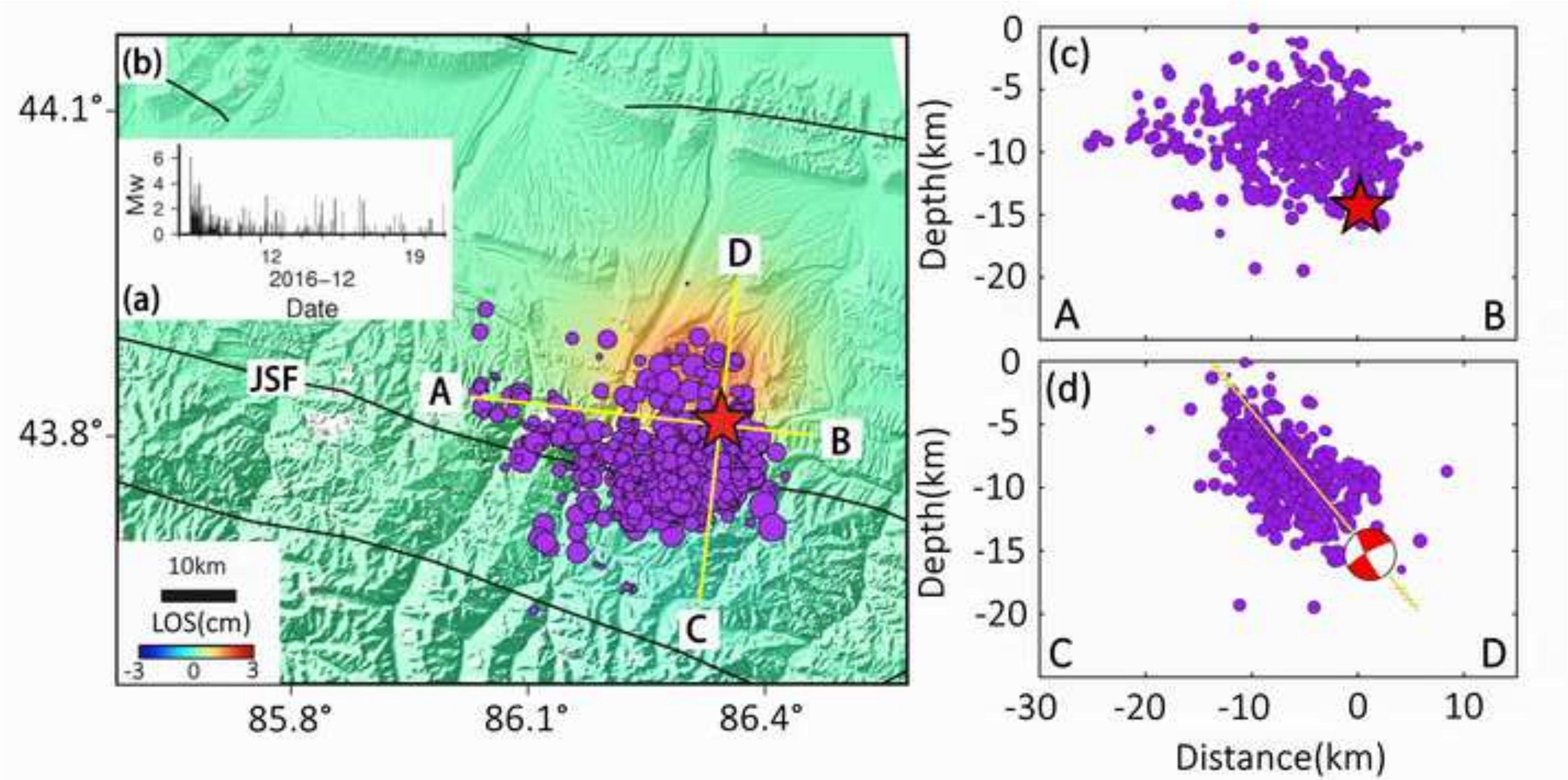

(b)
44.1°
43.8°
85.8°
86.1°
86.4°
Mw
6
4
2
0
12
19
2016-12
Date
(a)
JSF
A
B
C
D
10km
LOS(cm)
-3
0
3
(c)
(d)
Depth(km)
0
-5
-10
-15
-20
-30
-20
-10
0
10
Distance(km)

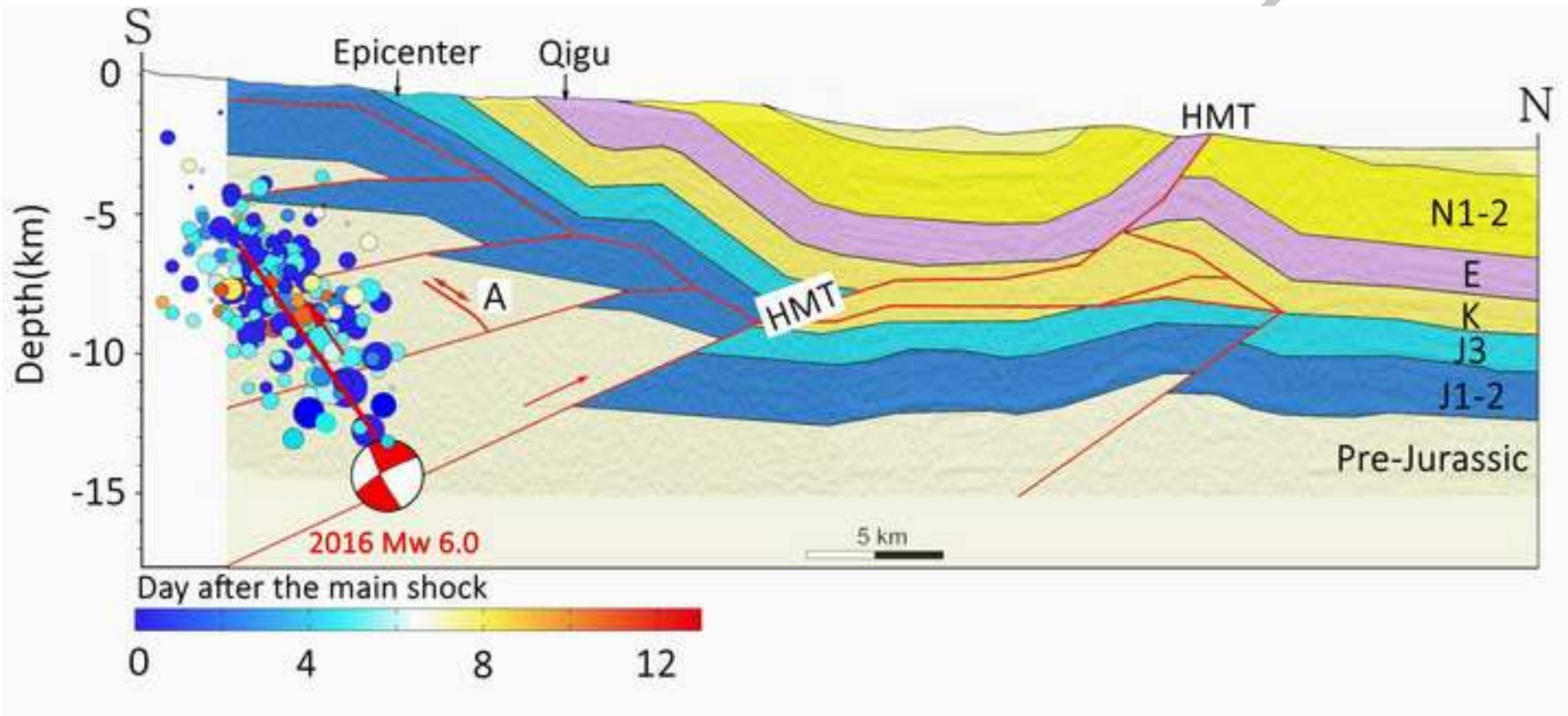
S
N
Epicenter
Qigu
HMT
HMT
A
N1-2
E
K
J3
J1-2
Pre-Jurassic
Depth(km)
0
-5
-10
-15
2016 Mw 6.0
5 km
Day after the main shock
0
4
8
12

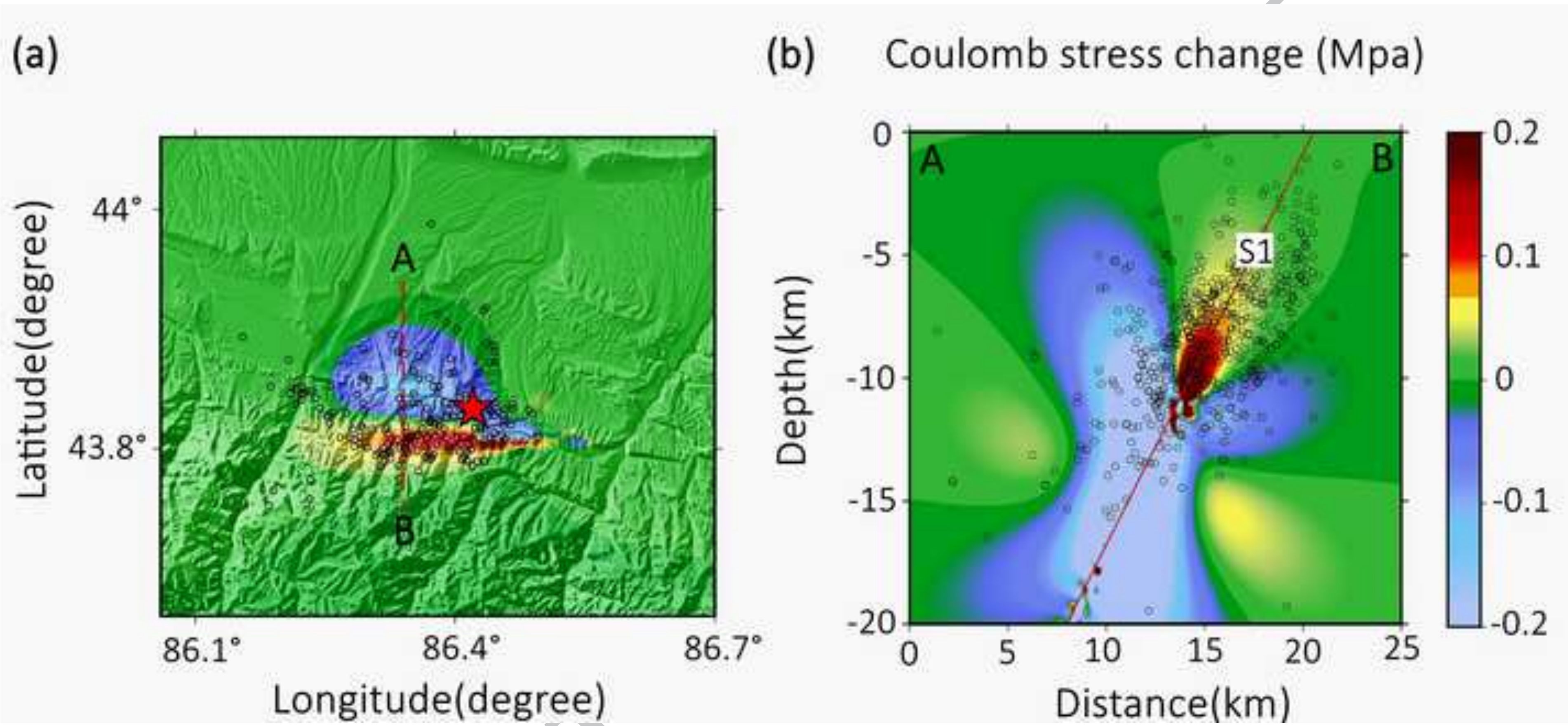
(a)
(b)
Coulomb stress change (Mpa)
A
B
44°
43.8°
86.1°
86.4°
86.7°
Latitude(degree)
Longitude(degree)
0
-5
-10
-15
-20
0
5
10
15
20
25
S1
Depth(km)
Distance(km)
0.2
0.1
0
-0.1
-0.2

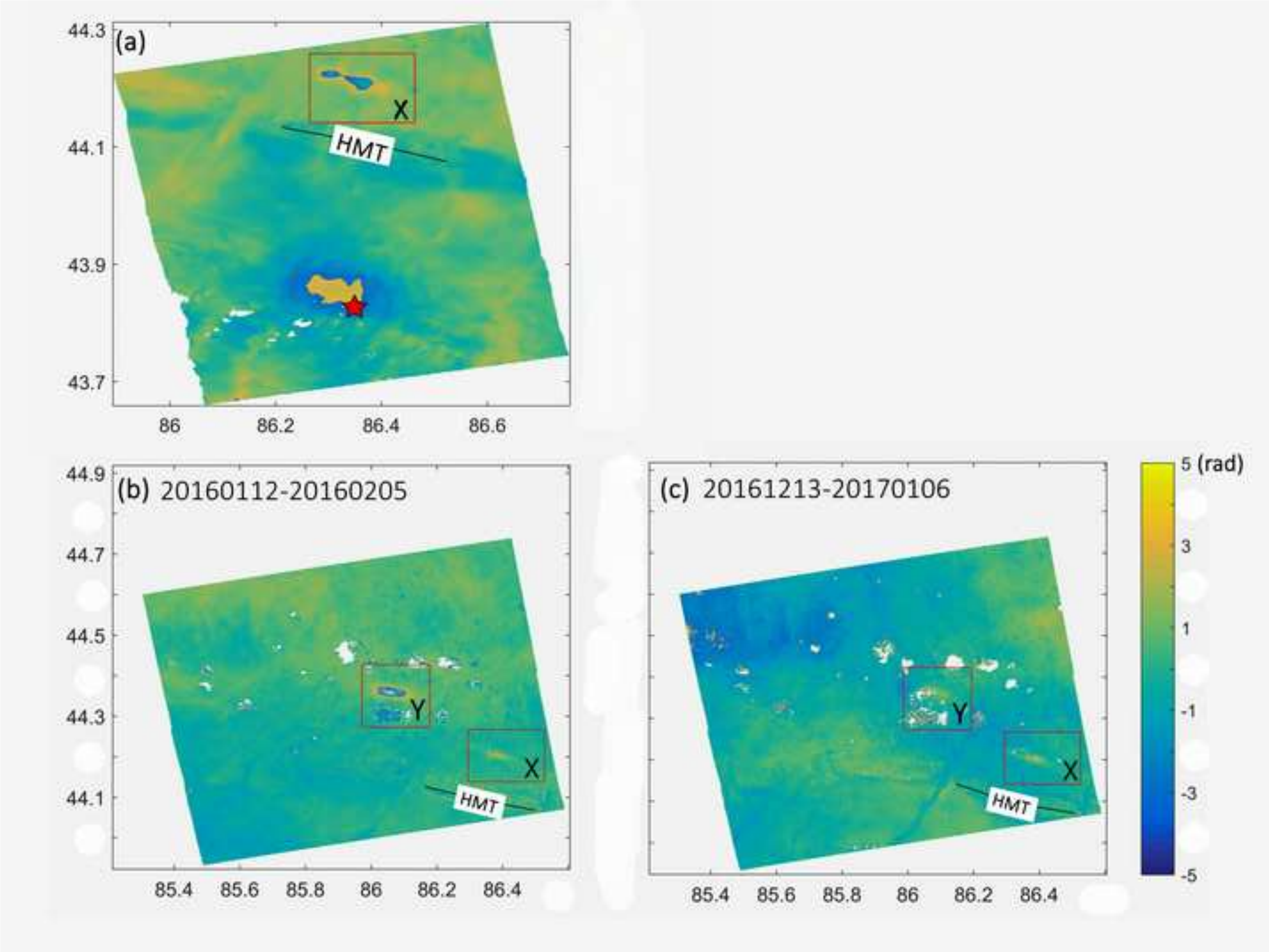
(a)
X
HMT
44.3
44.1
43.9
43.7
86
86.2
86.4
86.6
(b) 20160112-20160205
Y
X
HMT
44.9
44.7
44.5
44.3
44.1
85.4
85.6
85.8
86
86.2
86.4
(c) 20161213-20170106
Y
X
HMT
85.4
85.6
85.8
86
86.2
86.4
5 (rad)
3
1
-1
-3
-5

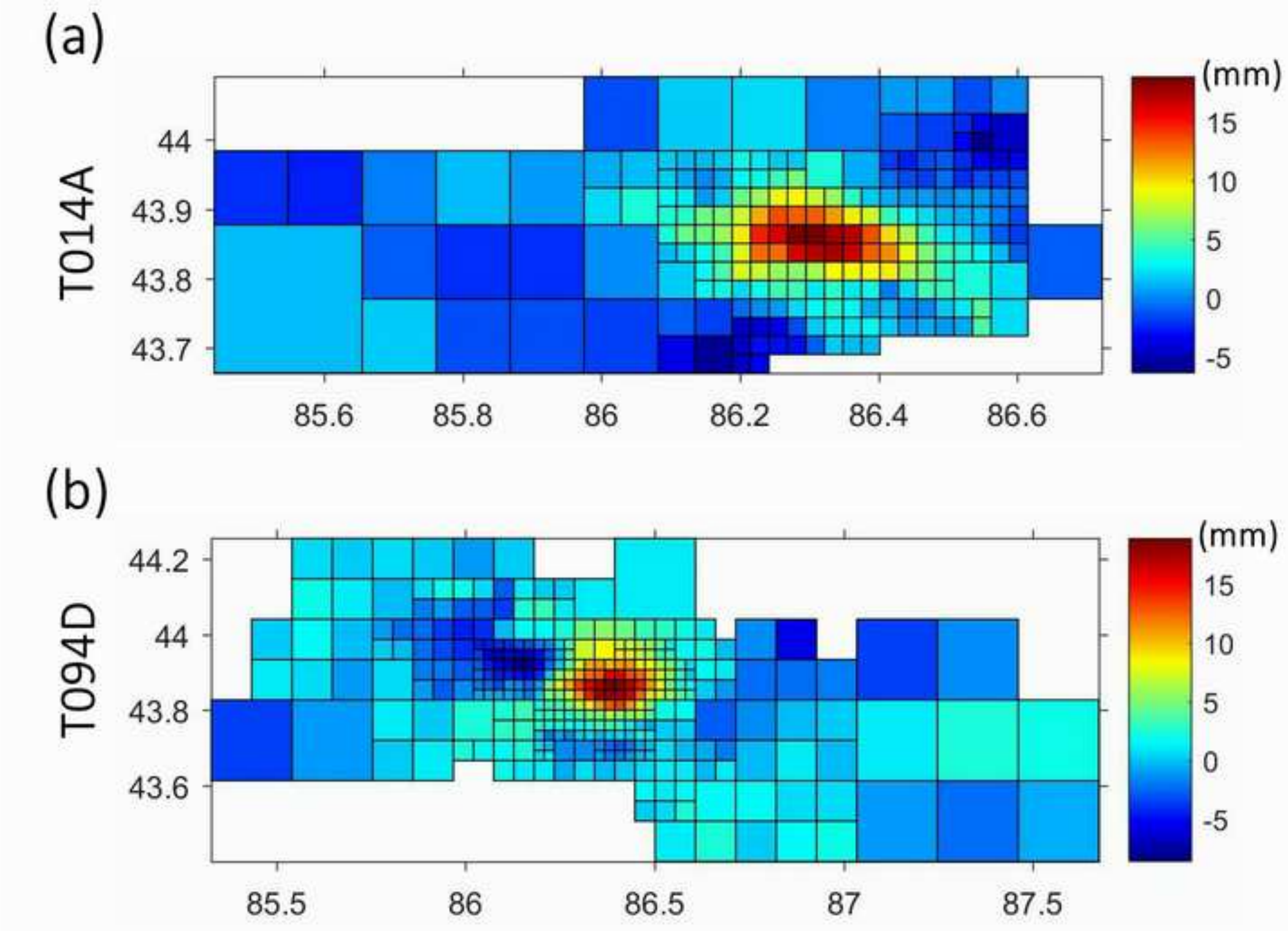

(a)
T014A
(mm)
15
10
5
0
-5
44
43.9
43.8
43.7
85.6
85.8
86
86.2
86.4
86.6
(b)
T094D
(mm)
15
10
5
0
-5
44.2
44
43.8
43.6
85.5
86
86.5
87
87.5

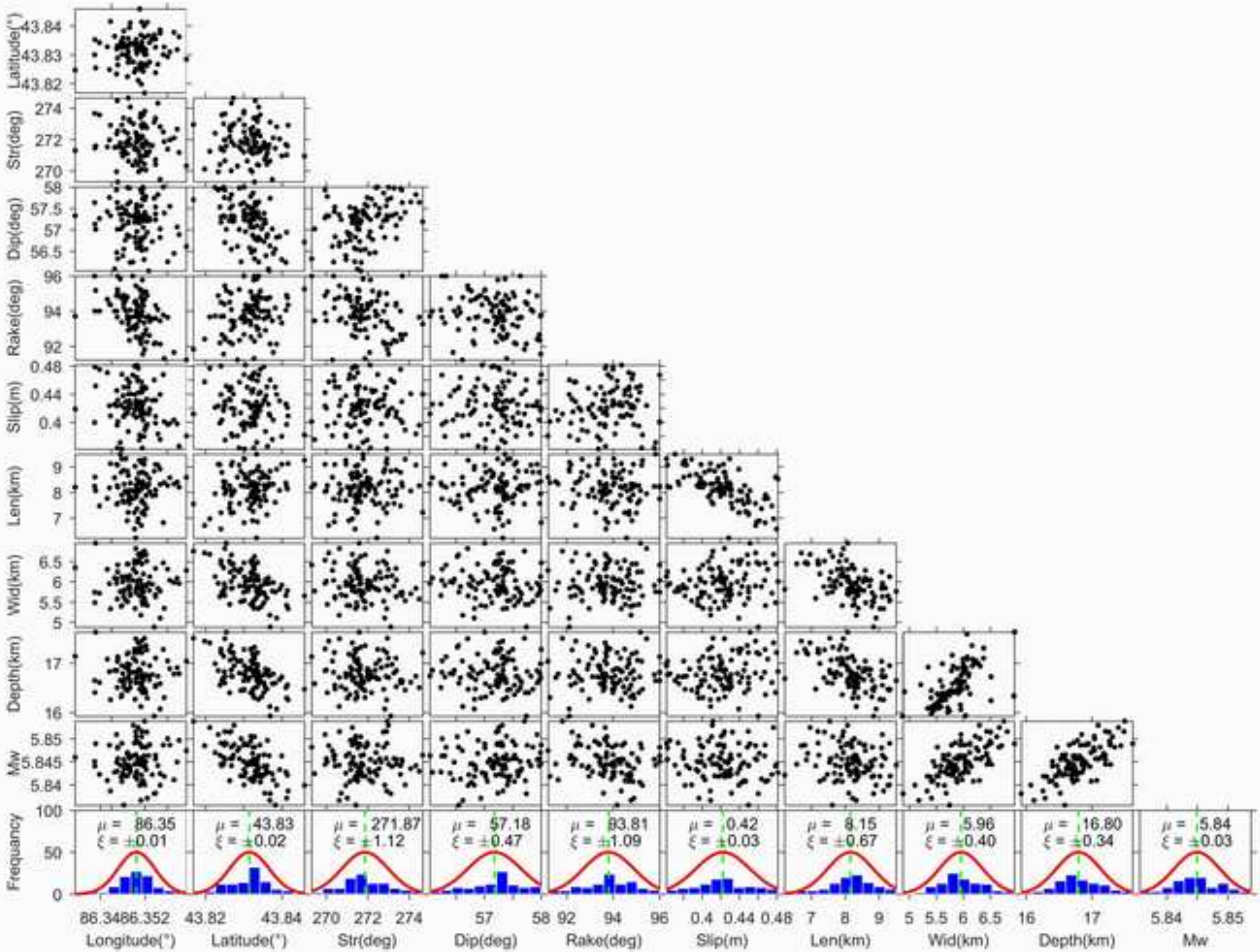
Latitude(°)
Str(deg)
Dip(deg)
Rake(deg)
Slip(m)
Len(km)
Wid(km)
Depth(km)
Mw
Frequency
μ = 86.35 ξ = ±0.01
μ = 43.83 ξ = ±0.02
μ = 271.87 ξ = ±1.12
μ = 57.18 ξ = ±0.47
μ = 93.81 ξ = ±1.09
μ = 0.42 ξ = ±0.03
μ = 8.15 ξ = ±0.67
μ = 5.96 ξ = ±0.40
μ = 16.80 ξ = ±0.34
μ = 5.84 ξ = ±0.03
Longitude(°)
Latitude(°)
Str(deg)
Dip(deg)
Rake(deg)
Slip(m)
Len(km)
Wid(km)
Depth(km)
Mw

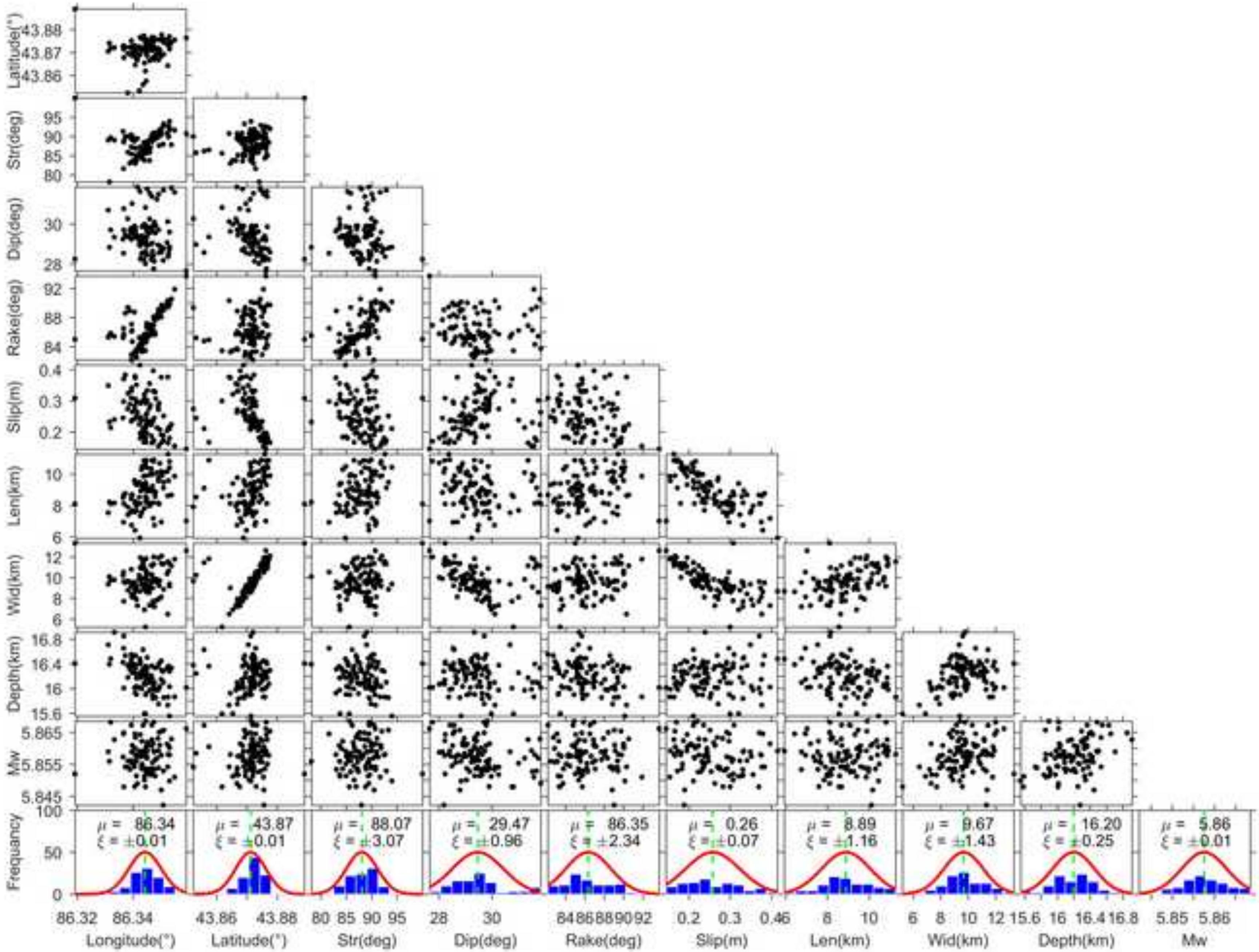

Latitude(°)
Str(deg)
Dip(deg)
Rake(deg)
Slip(m)
Len(km)
Wid(km)
Depth(km)
Mw
Frequency
μ = 86.34
ξ = ±0.01
μ = 43.87
ξ = ±0.01
μ = 88.07
ξ = ±3.07
μ = 29.47
ξ = ±0.96
μ = 86.35
ξ = ±2.34
μ = 0.26
ξ = ±0.07
μ = 8.89
ξ = ±1.16
μ = 9.67
ξ = ±1.43
μ = 16.20
ξ = ±0.25
μ = 5.86
ξ = ±0.01
Longitude(°)
Latitude(°)
Str(deg)
Dip(deg)
Rake(deg)
Slip(m)
Len(km)
Wid(km)
Depth(km)
Mw

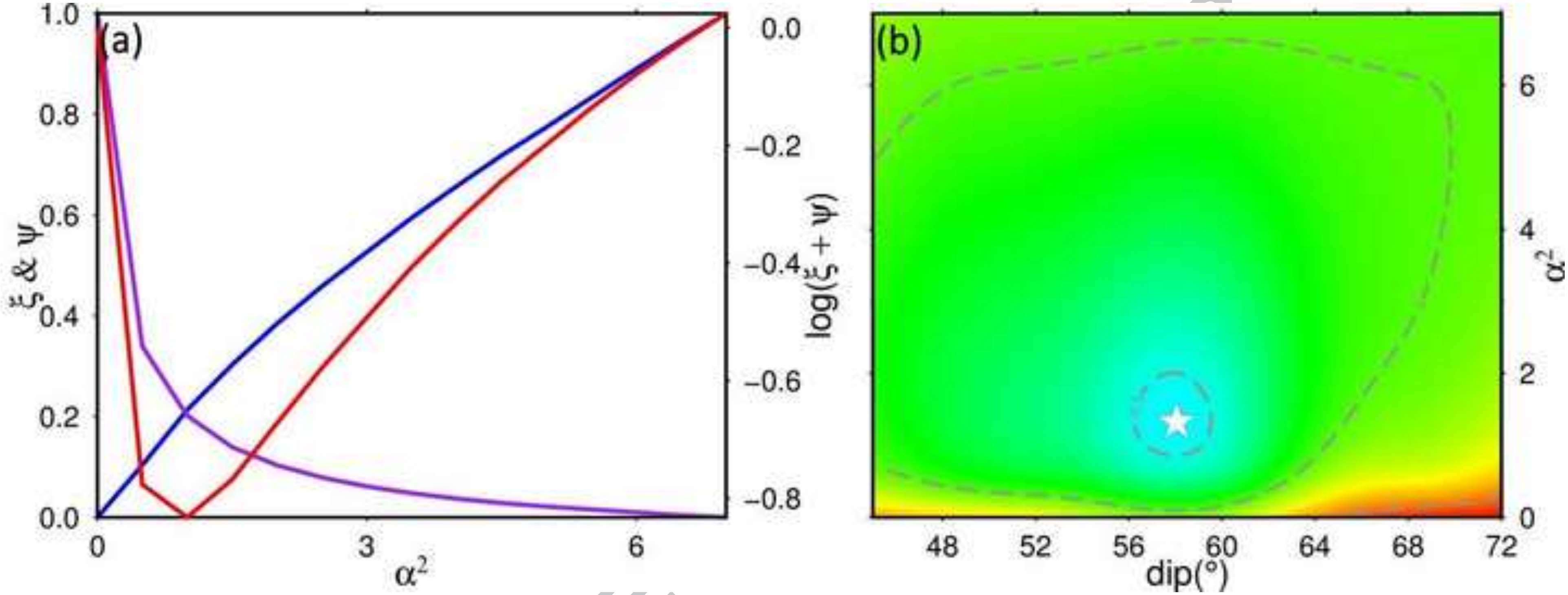
(a)
1.0
0.8
0.6
0.4
0.2
0.0
ξ & ψ
0
3
6
α²
0.0
−0.2
−0.4
−0.6
−0.8
log(ξ + ψ)
(b)
6
4
2
0
α²
48
52
56
60
64
68
72
dip(°)

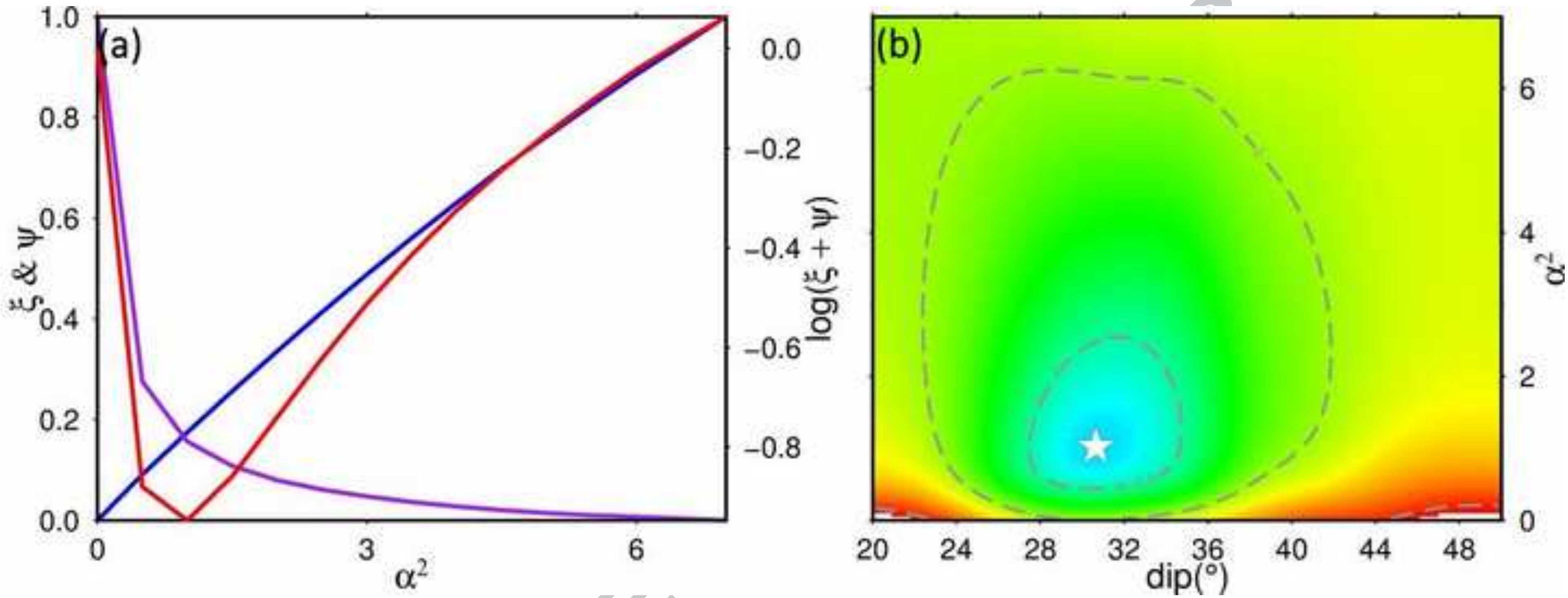
(a)
1.0
0.8
0.6
0.4
0.2
0.0
ξ & ψ
0
3
6
α²
0.0
−0.2
−0.4
−0.6
−0.8
log(ξ + ψ)
(b)
20
24
28
32
36
40
44
48
dip(°)
0
2
4
6
α²

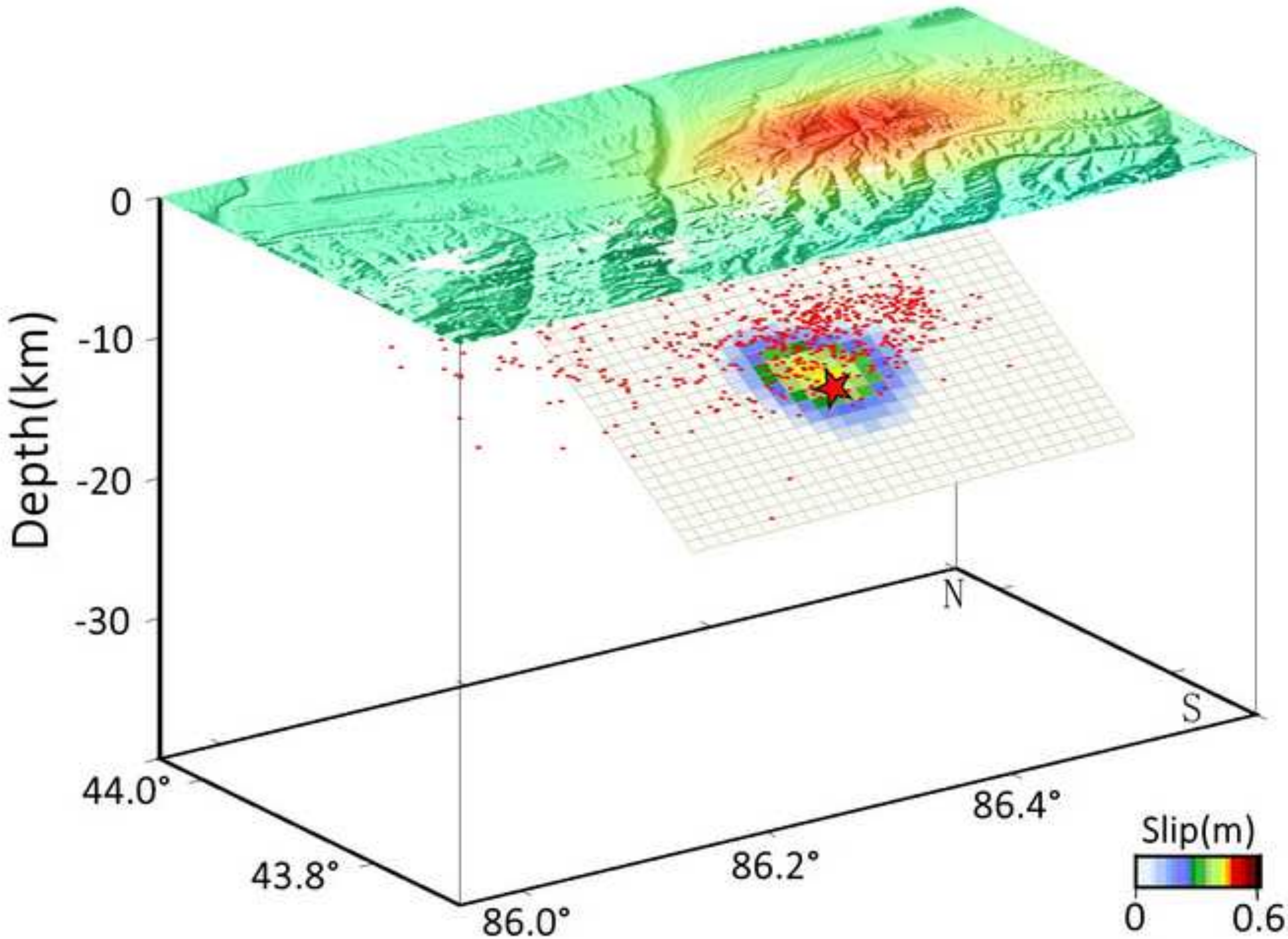

Depth(km)
0
-10
-20
-30
N
S
44.0°
43.8°
86.0°
86.2°
86.4°
Slip(m)
0
0.6

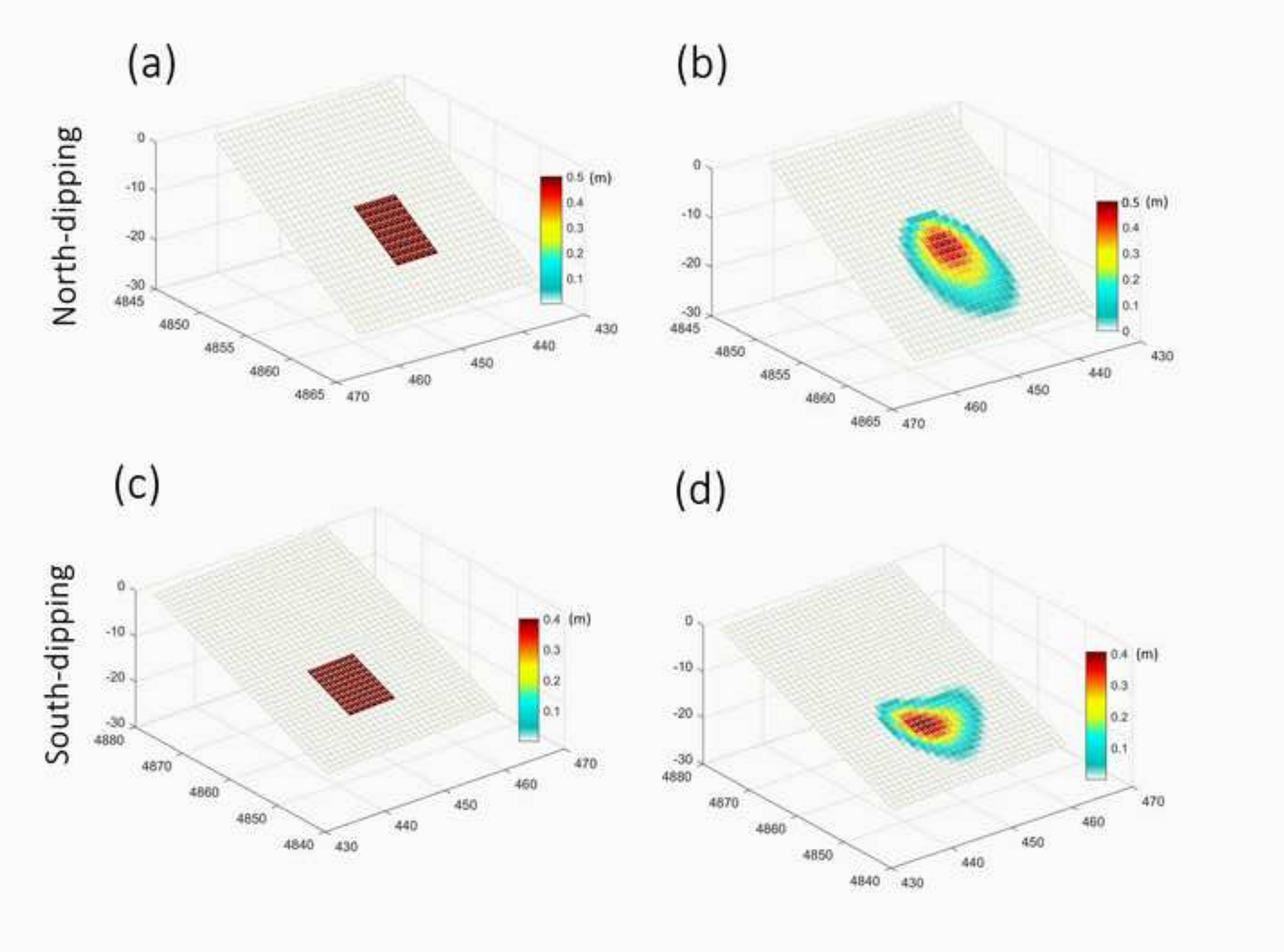
(a)
(b)
(c)
(d)
North-dipping
South-dipping
(m)

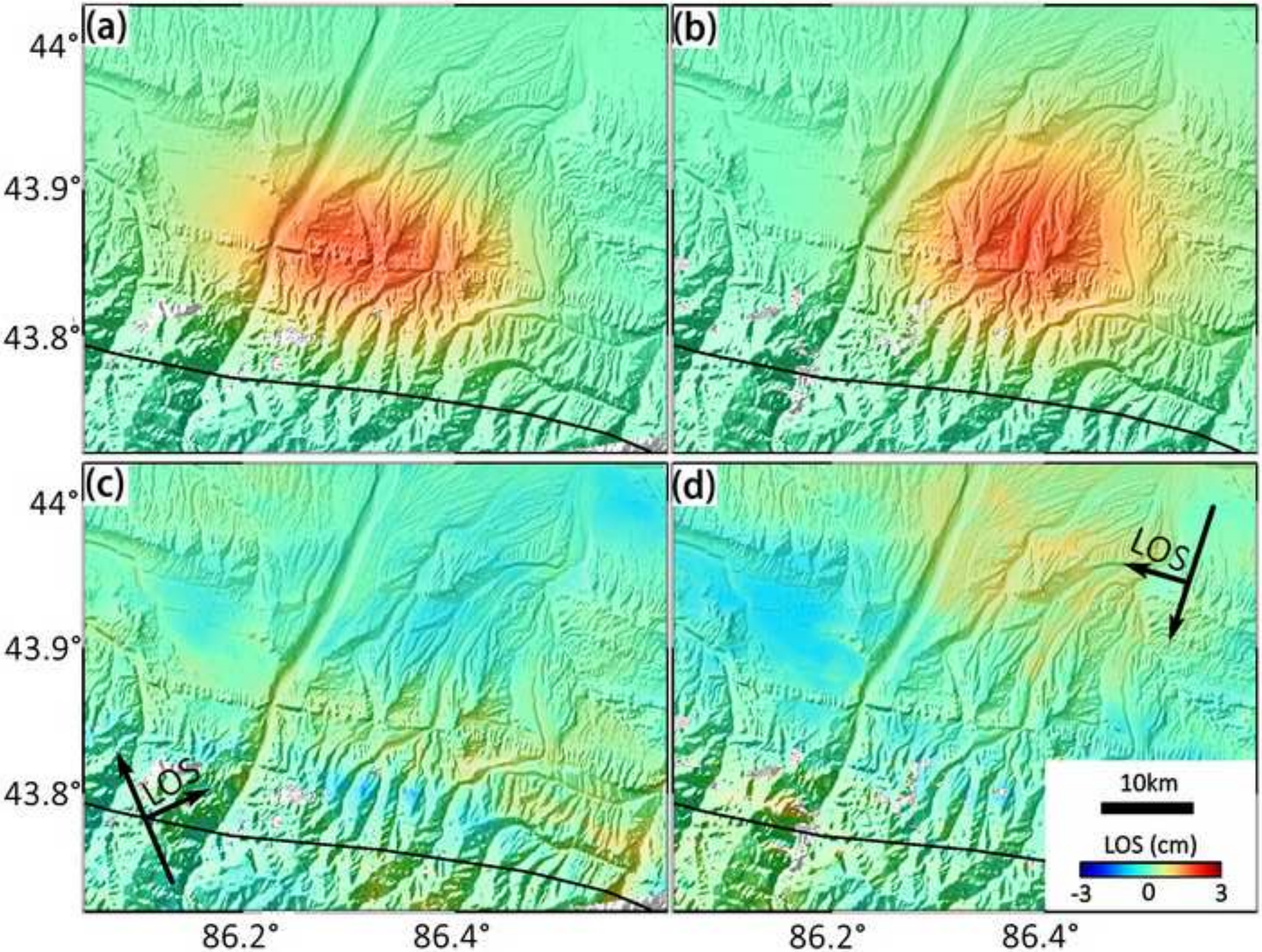
(a)
(b)
(c)
(d)
44°
43.9°
43.8°
86.2°
86.4°
LOS
10km
LOS (cm)
-3
0
3

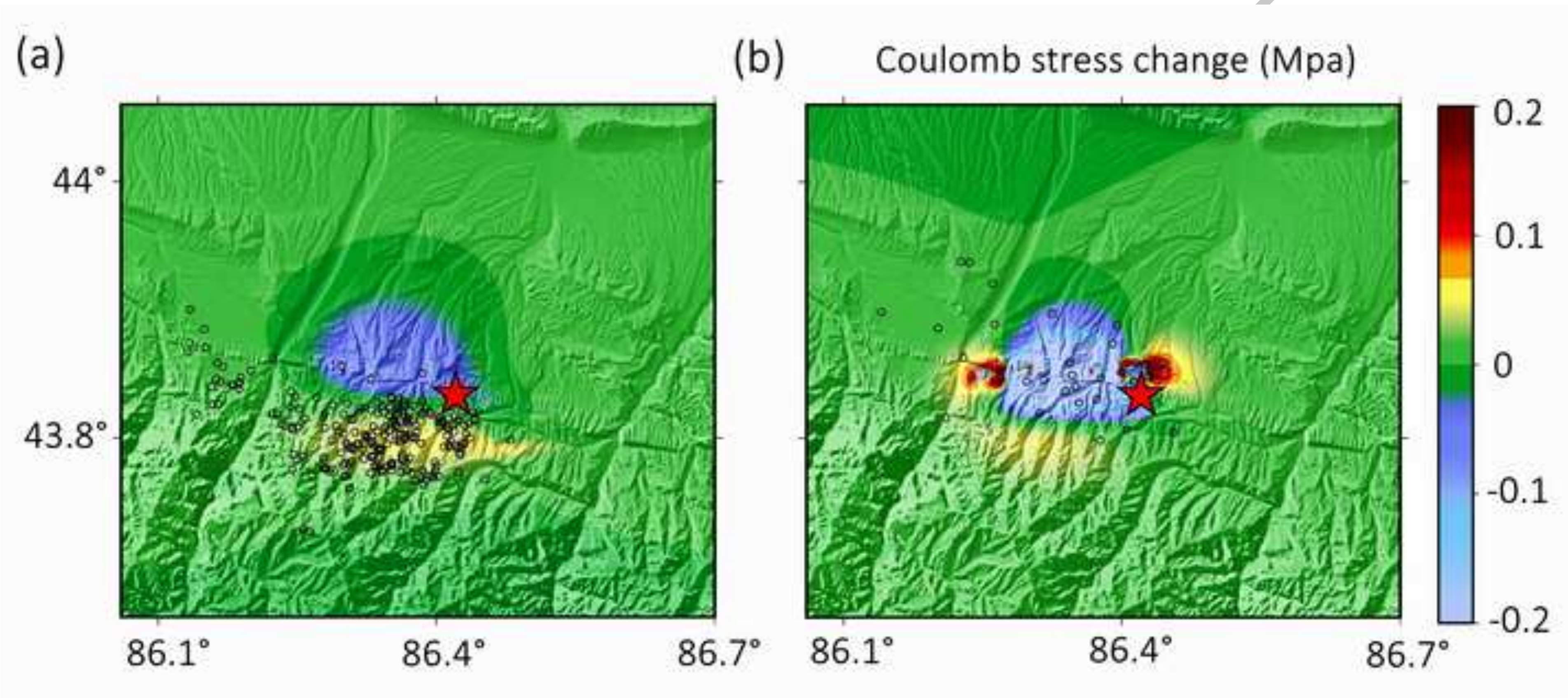
(a)
(b)
Coulomb stress change (Mpa)
44°
43.8°
86.1°
86.4°
86.7°
86.1°
86.4°
86.7°
0.2
0.1
0
-0.1
-0.2

Declaration of Interest Statement

We declared that we have no conflicts of interest to this work.

We declare that we do not have any commercial or associative interest that represents a conflict of interest in connection with the work submitted.

Author:

Xiaohang Wang[a], Caijun Xu[a,b,c,*], Yangmao Wen[a,b,c], Shuai Wang[a], Guangyu Xu[a], Zhuohui Xiao[a] and Lihua Fang[d]

a School of Geodesy and Geomatics, Wuhan University, Wuhan, China

b Key Laboratory of Geospace Environment and Geodesy, Ministry of Education, Wuhan University, Wuhan, China

c Collaborative Innovation Center of Geospatial Technology, Wuhan University, Wuhan, China

d Institute of Geophysics, China Earthquake Administration, Beijing, China

* Correspondence: cjxu@sgg.whu.edu.cn; Tel.: +86-27-6877-8805

Author contributions:

Xiaohang Wang performed the experiments, wrote and revised the manuscript; Caijun Xu and Shuai Wang designed the study, analyzed the experimental results and revised the manuscript; Yangmao Wen, Guangyu Xu and Zhuohui Xiao analyzed the experimental results and revised the manuscript. Lihua Fang provided the relocated aftershocks.

Conflicts of interest:

The authors declare that they have no competing interests.